Engineering Structures 240 (2021) 112093

Contents lists available at ScienceDirect

Engineering Structures

journal homepage: www.elsevier.com/locate/engstruct

Damage and sensitivity analysis of a reinforced concrete wall building during the 2010, Chile earthquake

José A. Gallardo *, Juan C. de la Llera *, Hernán Santa María, Matías F. Chacón

Department of Structural and Geotechnical Engineering, Pontificia Universidad Católica de Chile, Chile
Research Center for Integrated Disaster Risk Management (CIGIDEN), Chile

ARTICLE INFO

Keywords:
Building collapse
Non-linear finite element model
Continuum concrete model
Shear wall building
Uncertainty analysis

ABSTRACT

Buildings with Reinforced Concrete (RC) walls are commonly used to resist lateral forces in seismic countries because they provide high lateral stiffness and strength. In recent earthquakes, shear wall buildings have shown good behavior in general; however, a small percentage underwent severe damage localized typically in lower stories. Several numerical models have been developed and proposed to simulate the failure mechanism and behavior of RC walls. From the existing models, only those denoted as micro-models can accurately simulate the stress and strain distributions. The aim of this research is double: (i) to validate a nonlinear finite element wall model and the associated material stress-strain constitutive relationship using the behavior of a real building during the 2010 Chile earthquake; and (ii) to analyze the uncertainty of the response of the building due to changes in model parameters. To validate the response of the wall model, four experimental benchmark RC wall specimens were studied, and model accuracy was evaluated using five parameters: initial stiffness, peak base-shear, ultimate base-shear, maximum displacement, and dissipated energy. A sensitivity analysis was carried out to study the influence of material parameters in the wall response and its damage. The case-study is a 18-story building with 1 basement, which suffered severe damage during the 2010 Chile earthquake, which has been studied by non-linear response-history analysis. Uncertainty in the building response due to three important modeling assumptions was considered: Rayleigh's damping model parameters; effective elastic bending stiffness of the structural elements; and effect of the vertical ground motion component. Results showed that the proposed model can predict the seismic response of the building with reasonable accuracy by identifying correctly the damage location. This case-study enabled us to assess also the effect of damping in non-ductile structures, the important influence of the slab stiffness in the response, and the effect of the vertical ground motion component in the sequence of damaged walls.

1. Introduction

Reinforced Concrete (RC) shear walls are commonly used as lateral-force resistant systems for medium- to high-rise buildings in seismic countries such as Canada, Chile, Colombia, New Zealand, United States, and Turkey. It is because they have previously shown a good seismic performance, for instance, during the 1985 Chile earthquake where less than 10% of the buildings experienced moderate to severe damage [1]; the 2010 Chile earthquake with less than 2% of the buildings severely damaged [2]; the moderate earthquakes in Colombia in 1979, 1983, 1985, and 1999, in which the buildings presented only non-structural damage; the 2010 New Zealand earthquake in which 8% of RC wall buildings suffered moderate or severe damage [3]; the 2011 New Zealand earthquake, in which about 50% of the buildings presented moderate or severe damage [4]; and the 1999 and 2003 Turkey earthquakes with buildings suffering only minor nonstructural damage.

However, a new damage pattern was observed in some buildings during the 2010 Chile earthquake [5,6]. This damage pattern later repeated in structures in Christchurch during the 2011 New Zealand earthquake [4,7]. The failure is characterized by limited ductility with spalling of the concrete cover, buckling of the vertical reinforcement and crushing of the poorly confined concrete at the compression zone, which has been associated with simultaneous bending and compression of slender walls. Over this period, extensive research has been carried out to understand the behavior and failure mechanisms of the buildings during the 2010 Chile earthquake, which has lead to interesting

* Corresponding authors.
E-mail addresses: jogallardo@uc.cl (J.A. Gallardo), jcllera@ing.puc.cl (J.C. de la Llera).

https://doi.org/10.1016/j.engstruct.2021.112093
Received 4 December 2019; Received in revised form 8 February 2021; Accepted 19 February 2021
Available online 3 May 2021

findings. Different researchers have studied one of the collapsed building in detail [2]. For instance, Song et al. [8] discussed the plausible causes of the collapse of this building; Maffei et al. [9] showed that concrete crushing triggered the collapse, and bar buckling occurred after concrete spalling; Deger and Wallace [10] studied concrete crushing in T-shape walls and initially concluded that the failure mechanism was undetermined; however, subsequent research determined that collapse was triggered by concrete crushing [11,12]. Westenenk et al. [13] studied other 8 buildings among them the case study of this research and concluded that failure started at the boundaries due to high axial stresses. Additionally, Ugalde and Lopez-Garcia [14] studied two undamaged buildings to understand their lack of damage, concluding that it was consequence of foundation uplift.

Real data of building performance during these and others seismic events is still scarce due mainly to the infrequent occurrence of large earthquakes and the small number of wall instrumented buildings. Examples of data collected from these events are photographs, technical reports, and some aftershock instrumentation of damaged buildings [15,16]. To partially solve this problem, several experimental campaigns have been carried out in the last forty years by different researchers to understand the seismic behavior and failure mechanism of typical RC building walls. These tests have been performed for walls with different geometries, such as rectangular walls without openings [17–20]; walls with regular and staggered openings [21,22]; flanged walls with T-, C-, and U-shapes [23,24], and flanged walls with regular and staggered openings [25]. Furthermore, these experimental tests enabled the calibration of numerical models to predict the inelastic behavior of RC walls under different load patterns.

Different numerical models have also been developed to simulate the nonlinear response of RC walls. These models can be classified, according to the modeling approach used, in two main groups: macro-models and micro-models. Macro-models represent walls by a set of simplified nonlinear elements, which simulate the phenomenological behavior of concrete, steel bars, and they interaction under cyclic loads. Examples of these models are the zero-length rotational spring, and zero-length fiber hinge element [26–28]; fiber-type beam-column elements, and the fiber-type beam-column elements with flexure-shear interaction [29–33]. Micro-models (also called continuum models) are based generally on Finite Element (FE) formulations. For this class of models, concrete and steel bars are simulated as independent elements to estimate the stress and strain distribution along the entire element at the expense of a high computational cost. Examples are the solid brick element [34,35]; the fiber-shell element; and the layered-shell element [36]. Several technical reports and codes provide information on how to model RC walls using both approaches. Such is the case of NIST GCR 17–917-45 [37], which also presents a thorough comparison between wall modeling methods. Researchers in the past have also compared and quantified the effect of different modeling assumptions in the performance of RC walls (epistemic uncertainty), such as: concentrated and distributed plasticity elements versus shell element models [38]; different concentrated plasticity elements [28]; and shell versus solid brick FE types [39].

These numerical RC wall models have been used for the modeling of individual walls, as well as to predict the behavior of complete RC wall buildings. For instance, Lu et al. [40] used a multi-layer shell elements to simulate the collapse process of a building, and later [41] used the same element model to simulate the behavior of super-tall buildings; Jünemann et al. [42] first analyzed resisting planes of a building using nonlinear shell elements, and later a complete structure using the model proposed by Vásquez et al. [26]; and Lu and Panagiotou [43] simulated the behavior of a simple building using a beam-truss model [44].

In Non-linear Response History (NRH) analysis of buildings, the damping and the effective stiffness of elastic elements are two very relevant parameters that significantly influence the predicted response. Both parameters somehow account the mild inelastic behavior (i.e. concrete cracking and rebar yielding) of structural elements modeled as elastic. While damping represents the energy dissipation, the effective stiffness indirectly consider cracking and some eventual element softening. Codes provide information about approaches of modeling damping ratios, and element cross-section effective stiffness, expressed as a percentage of the gross stiffness EI_g [45–48]. In addition, several authors have studied the influence of these parameters in the building response. Some have computed the damping ratio of structures from experimental ambient vibration measures using different techniques [49,50]; or studied the change in dynamic building properties in pre- and post-earthquake [16]; or analyzed the influence of the damping model in the response [49,51]. Furthermore, the effects of the vertical component of ground motion is not considered yet in most codes, but only in special cases [48,47]. Despite the vast research and progress about these topics, there is still no consensus on what is correct for building modeling. Indeed, all these different assumptions are still a significant source of uncertainty and these parameters are key in predicting the response, especially in buildings with limited ductility.

Consequently, this research aims to study and validate a Non-linear Reinforced Concrete Wall (NRCW) finite element model using experimental results of wall tests, and the behavior of a real RC shear wall building damaged during the 2010 Chile earthquake. An additional aim is to predict wall damage, and evaluate the variability observed due to different dynamic parameters, such as the Rayleigh's damping coefficients, effective elastic bending stiffness of slabs and walls, and the vertical ground motion component. In Section 2, the NRCW model, its element formulation for concrete and steel, and the constitutive model for both materials are presented. In Section 3, the model is validated using the experimental results of four tested RC walls. Section 4 does a sensitivity analysis of material parameters for the response of four RC benchmark wall models. Section 5 uses the NRCW model to analyze the inelastic behavior of an actual RC wall building damaged during the 2010 Chile earthquake using NRH analysis. Section 6 presents a sensitivity analysis of the building response for three dynamic parameters: (i) Rayleigh damping coefficients; (ii) effective bending stiffness of slabs and walls; and (iii) vertical component of ground motion. Finally, conclusions are presented for this research.

2. NRCW finite element model

This section briefly describes the NRCW finite element model used to predict the inelastic behavior of RC wall elements, which is used later for the dynamic response of the RC wall building. The model corresponds to a sandwich of layered-shell elements of concrete and steel rebar elements, which stress-strain constitutive models are included in Ansys [52]. The concrete model is the plastic damage model proposed by Faria et al. [53], whereas the steel model is the well-known model proposed by Menegotto-Pinto [54] with a minor modification that enables to consider different yield strengths in compression and tension.

2.1. Element models

Layered-shell (SHELL181) elements are used to simulate concrete behavior. Each element is defined by 4 (or 3) nodes with six Degrees-of-Freedom (DOFs) per node using the Bathe-Dvorkin formulation [55]. The wall cross-section is subdivided into a specific number of layers through thickness, which accommodates the geometry of the reinforcement layers. Three integration points are located (Fig. 1) through the thickness of each layer, two located at the external surfaces respectively, and one at the center of each layer as shown in Fig. 1. Moreover, for each integration point in each layer a plane-stress material formulation is considered.

The reinforcement is embedded and defined relative to the base element (Fig. 1). It can be modeled as discrete (REINF264), in which each bar has a cross-section area with a uniaxial stress-strain material behavior, and is individually placed within the base element. As an alternative, reinforcement can be modeled as smeared elements

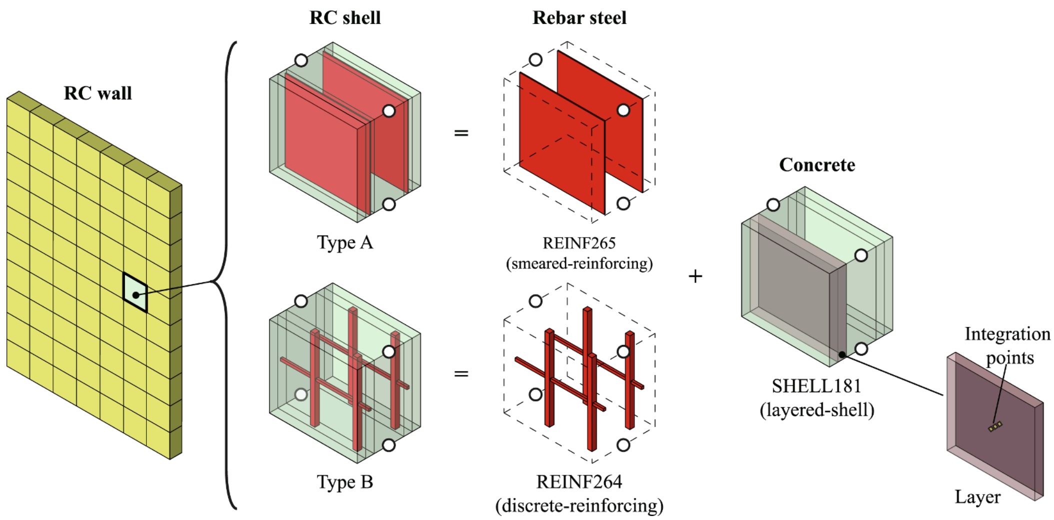

Fig. 1. Finite element types and their assemblage.

(REINF265), where the rebar of the section is distributed in a layer of equivalent area inside the base element. Each reinforcing layer has a unique orientation, material, and cross-section area, and is simplified as a homogeneous uniaxial membrane. In both approaches, rebars develop an uniaxial straight behavior perfectly bonded with the base element, thus neglecting rebar buckling, dowel-action and the bond-slip effect. A sensitivity analysis was performed with wall $W2$ (see later), which was modeled using both reinforcement elements (REINF264 and REINF265) in order to evaluate the two options of rebar modeling. The boundary conditions and the history of lateral displacements applied at the top of the wall were similar for both models, and a static analysis was perform with displacement control. Because the damage location and global response of the wall model showed negligible differences between both configurations [56], a smeared reinforcement approach was chosen for all cases.

2.2. Concrete and steel constitutive models

2.2.1. Concrete

The plastic-damage constitutive model proposed by Faria et al. [53] was selected to simulate concrete behavior, which is based on the theory of plasticity and continuum damage mechanics. For this model, Faria et al. [53] defines the Cauchy stress tensor $\boldsymbol{\sigma}$ as

$$\boldsymbol{\sigma} := (1-\omega^+)\bar{\boldsymbol{\sigma}}^+ + (1-\omega^-)\bar{\boldsymbol{\sigma}}^-, \tag{1}$$

where $\omega^{\pm}$ are the tensile/compressive damage variables, respectively; $\bar{\boldsymbol{\sigma}}^+$ and $\bar{\boldsymbol{\sigma}}^-$ are the tensile and compressive components of the effective stress tensor $\bar{\boldsymbol{\sigma}}$, respectively, which are obtained through a spectral decomposition. According to Ortiz [57], this spectral decomposition can be written as

$$\bar{\boldsymbol{\sigma}}^{\pm} := \sum_{i=1}^{N} \langle \hat{\bar{\sigma}}_i \rangle^{\pm} \boldsymbol{E}_{\bar{\boldsymbol{\sigma}}}^{ii} = \boldsymbol{\mathcal{P}}^{\pm} : \bar{\boldsymbol{\sigma}}, \qquad \text{with} \tag{2a}$$

$$\boldsymbol{\mathcal{P}}^{\pm} = \sum_{i=1}^{N} H_0^{\pm}(\hat{\bar{\sigma}}_i)\left(\boldsymbol{E}_{\bar{\boldsymbol{\sigma}}}^{ii} \otimes \boldsymbol{E}_{\bar{\boldsymbol{\sigma}}}^{ii}\right) \qquad \text{and} \qquad \boldsymbol{E}_{\bar{\boldsymbol{\sigma}}}^{ii} = \underline{\boldsymbol{v}}^i \otimes \underline{\boldsymbol{v}}^i, \tag{2b}$$

where $\hat{\bar{\sigma}}_i$, $\boldsymbol{v}^i$, and $\boldsymbol{E}_{\bar{\boldsymbol{\sigma}}}^{ii}$ are the i-th eigenvalue, eigenvector, and eigenprojector of the effective stress tensor $\bar{\boldsymbol{\sigma}}$; $\boldsymbol{\mathcal{P}}^{\pm}$ are the positive/negative fourth-order projection tensors, respectively; $\langle \bullet \rangle^{\pm}$ are the positive/negative Macauley functions, respectively, (i.e., $\langle x \rangle^{\pm} = (x \pm |x|)/2$); $H_0^{\pm}(\bullet)$ denotes the positive/negative Heaviside functions (1 if $(\bullet) > 0$, and 0 if $(\bullet) \leq 0$ for the positive function, and the opposite for the negative function), respectively; the symbol $\otimes$ denotes the outer tensor product; the symbol " : " is the inner double tensor product or contraction; and N denotes the dimension of the second-order tensor (i.e., $N = 3$ for the 3D case and $N = 2$ for plane-stress). This decomposition satisfies the relations $\bar{\boldsymbol{\sigma}} = \bar{\boldsymbol{\sigma}}^+ + \bar{\boldsymbol{\sigma}}^-$ and $\boldsymbol{\mathcal{P}}^+ + \boldsymbol{\mathcal{P}}^- = \boldsymbol{\mathcal{I}}$, where $\boldsymbol{\mathcal{I}}$ is the fourth-order identity tensor.

In addition, an independent positive and negative damage criterion needs to be defined, which is expressed by [58]

$$F_d^{\pm}(Y^{\pm}, r^{\pm}) := Y^{\pm} - r^{\pm} \leqslant 0, \tag{3}$$

where $Y^{\pm}$ are the tensile/shear thermodynamic forces (or damage energy release rate), which are defined to drive the forces of the internal damage variables; and $r^{\pm}$ are the tensile/compressive damage thresholds. Simo and Ju [59] defined $Y^{\pm}$ as

$$Y^{\pm} = \sqrt{E_c\left(\bar{\boldsymbol{\sigma}}^{\pm} : \boldsymbol{\mathcal{C}}^e : \bar{\boldsymbol{\sigma}}^{\pm}\right)}, \tag{4}$$

where E_c is the concrete Young's modulus and $\boldsymbol{\mathcal{C}}^e$ is the fourth-order linear elastic compliance tensor. Moreover, the damage thresholds $r^{\pm}$ are increasing functions that satisfy the following relations [60]

$$r^{\pm} = \max\left(r_o^{\pm}, \max_{[0,t]}(Y^{\pm})\right) \qquad \text{and} \tag{5a}$$

$$\dot{r}^{\pm} = \dot{Y}^{\pm}, \tag{5b}$$

where $r_o^{\pm}$ represents the initial damage threshold. Assuming uniaxial behavior, these values can be calculated as $r_o^{\pm} = \sigma_o^{\pm}$, where $\sigma_o^{\pm}$ are the stresses beyond which nonlinearity becomes visible under uniaxial tension and compression, respectively.

The effective stress tensor $\bar{\boldsymbol{\sigma}}$ is defined by

$$\bar{\boldsymbol{\sigma}} := \boldsymbol{\mathcal{D}}^e : \varepsilon^e = \boldsymbol{\mathcal{D}}^e : (\varepsilon - \varepsilon^p), \tag{6}$$

where $\boldsymbol{\mathcal{D}}^e$ denotes the usual fourth-order isotropic linear-elastic stiffness tensor; and $\boldsymbol{\varepsilon}, \boldsymbol{\varepsilon}^e$, and $\boldsymbol{\varepsilon}^p$ are the total, elastic, and plastic second-order strain tensors, respectively, with $\boldsymbol{\varepsilon} = \boldsymbol{\varepsilon}^e + \boldsymbol{\varepsilon}^p$. Faria et al. [53] defined a simple expression for the evolution law of the plastic strain tensor as

$$\dot{\boldsymbol{\varepsilon}}^p := \dot{\gamma}\bar{\boldsymbol{\sigma}}, \text{ with} \tag{7a}$$

$$\dot{\gamma} = E_c \lambda \frac{\langle \boldsymbol{\varepsilon}^e : \dot{\boldsymbol{\varepsilon}} \rangle}{(\bar{\boldsymbol{\sigma}} : \bar{\boldsymbol{\sigma}})} \tag{7b}$$

where $\lambda = B^+ H_o^+(\dot{\omega}^+) + B^- H_o^+(\dot{\omega}^-) \geqslant 0$ is a material parameter that controls the rate intensity of plastic deformation, and $B^{\pm} \in [0, 1[$ are the

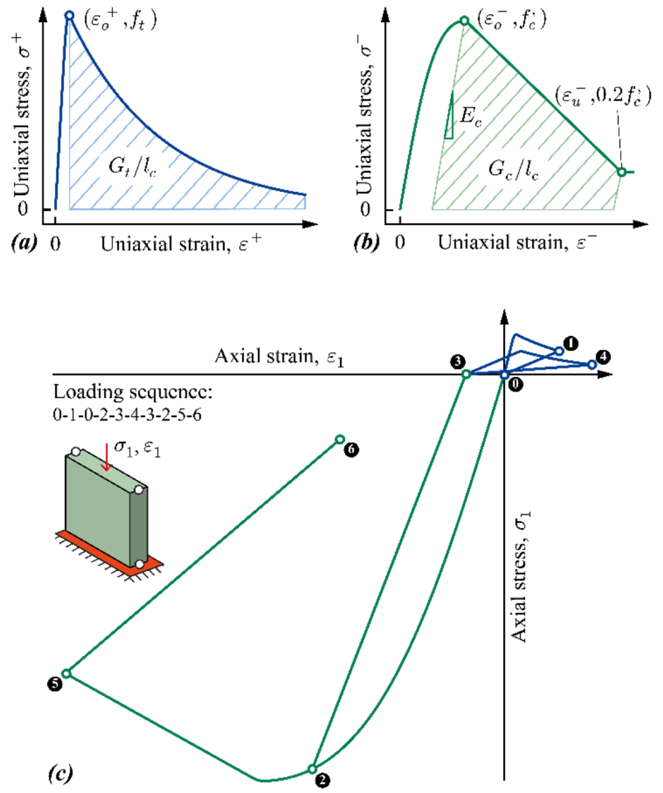

Fig. 2. Sketches of the uniaxial stress-strain laws of the concrete model in: (a) compression; (b) tension; and (c) cyclic loading.

positive/negative plastic factors, respectively. Note that for the plane-stress case, the flow rule given by Eq. 7a leads to an out-of-plane plastic strain ε_{33}^p=0.

The damage variables $\omega^{\pm}$ are a function of the damage thresholds [58] (i.e., $\omega^{\pm} = \omega^{\pm}(r^{\pm})$). However, since experimentally, $\sigma^{\pm}(\varepsilon^{\pm})$ are well known for concrete, it is necessary a relation between $\sigma^{\pm}(\varepsilon^{\pm})$ and $\omega^{\pm}(r^{\pm})$. Recently, Chacón [58] established such transformation as

$$\omega^{\pm}(r^{\pm}) := 1 - \frac{1}{r^{\pm}}\sigma^{\pm}\left(\frac{r^{\pm}}{E_c}\right), \qquad \text{and} \tag{8a}$$

$$\frac{d\omega^{\pm}(r^{\pm})}{dr^{\pm}} = \left[\sigma^{\pm}\left(\frac{r^{\pm}}{E_c}\right) - \frac{r^{\pm}}{E_c}\frac{\partial\sigma^{\pm}(\varepsilon^{\pm})}{\partial\varepsilon^{\pm}}\right]\frac{1}{(r^{\pm})^2}. \tag{8b}$$

Additionally, the model includes a strain-rate component to improve considerably the numerical convergence in strain-softening regimes. The Duvaut-Lions visco-plastic model [61] is considered to evaluate the visco-plastic strains $\boldsymbol{\varepsilon}^{vp}$ and the effective viscous stress tensor $\bar{\boldsymbol{\sigma}}^{v}$ as follows

$$\dot{\varepsilon}^{vp} = \frac{1}{\mu_v}\mathcal{C}^e : (\bar{\boldsymbol{\sigma}}^v - \bar{\boldsymbol{\sigma}}), \tag{9a}$$

$$\bar{\boldsymbol{\sigma}}^v = \mathcal{D}^e : (\varepsilon - \varepsilon^{vp}). \tag{9b}$$

Thus, the nominal viscous stress tensor $\boldsymbol{\sigma}^v$, and the damage thresholds variables $r^{\pm}$ are redefined according to the following expressions

$$\boldsymbol{\sigma}^v := (1-\omega^+)\bar{\boldsymbol{\sigma}}^{v+} + (1-\omega^-)\bar{\boldsymbol{\sigma}}^{v-}, \text{ with} \tag{10a}$$

$$\bar{\boldsymbol{\sigma}}^{v\pm} = \mathcal{P}_v^{\pm} : \bar{\boldsymbol{\sigma}}^v, \qquad \mathcal{P}_v^{\pm} = \sum_{i=1}^{N} H_0^{\pm}(\hat{\bar{\sigma}}_i^v)\left(\boldsymbol{E}_{\bar{\sigma}^v}^{ii} \otimes \boldsymbol{E}_{\bar{\sigma}^v}^{ii}\right), \text{ and} \tag{10b}$$

$$\dot{r}^{\pm} = -\frac{1}{\mu_v}(r^{\pm} - Y^{\pm}), \tag{10c}$$

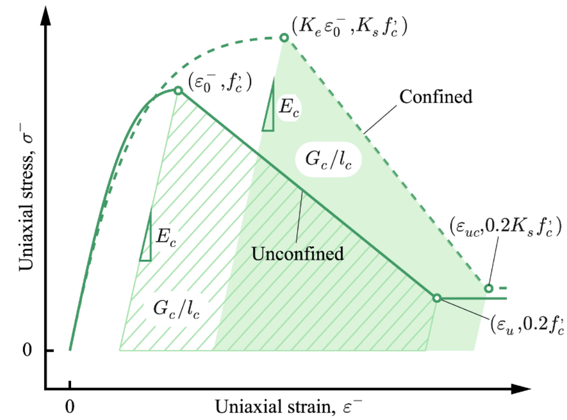

Fig. 3. Sketches of the uniaxial confined and unconfined stress-strain laws of the concrete model.

where μ_v is the numerical viscosity factor (i.e. the relaxation time in visco-plastic models).

In summary, the input parameters for this model are: (i) the positive B^+ and negative B^- plasticity factors; (ii) numerical viscosity μ_v (0.5 was used in all analysis); and (iii) the uniaxial tensile/compressive stress-strain laws. The model used for the uniaxial response in compression is the one defined by Saatcioglu-Razvi [62] (Fig. 2b). This model uses three parameters to define the stress-strain curve: the uniaxial peak compressive strength $f_c^{\prime}$; the concrete Young's modulus E_c; and the compressive fracture energy per unit area G_c (the strain at the peak strength ε_o^- is defined as $\varepsilon_o^- = 2f_c^{\prime}/E_c$). For the uniaxial concrete response in tension, the exponential model of Oliver et al. [63] is used (Fig. 2a), where the required parameters are: the uniaxial tensile strength f_t; the concrete Young's modulus E_c, identical as in compression; and the tensile fracture energy per unit area G_t (the strain at peak tensile strength is defined as $\varepsilon_o = f_t/E_c$). Finally, both uniaxial stress-

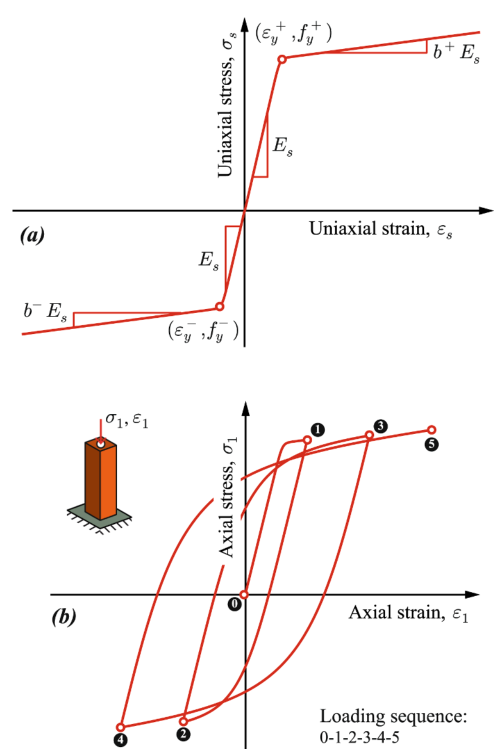

Fig. 4. Sketches of the stress-strain laws of the steel model in: (a) tension; and (b) cyclic loading.

Table 1
General characteristics of the experimental RC wall specimens (l_w= wall length; h_w= wall height; t_w= wall thickness; ρ_v= vertical reinforcement ratio; ρ_h= horizontal reinforcement ratio; ρ_b= volumetric reinforcement ratio of the confined boundary elements; and η_w= axial load ratio).

Specimen	Wall name	Authors	l_w [cm]	h_w [cm]	t_w [cm]	h_w/l_w [–]	ρ_v [%]	ρ_h [%]	ρ_b [%]	η_w [%]
W1	M3	Amon [20]	90	200	15	2.22	0.89	0.25	2.15	10.0
W2	WSH4	Dazio et al. [17]	200	456	15	2.28	0.82	0.25	1.54	6.0
W3	RW-A20-P10-S63	Tran [18]	122	244	15	2.00	2.83	0.61	7.11	7.0
W4	RW2	Thomsen et al. [24]	122	366	10	3.00	1.12	0.33	2.93	9.0

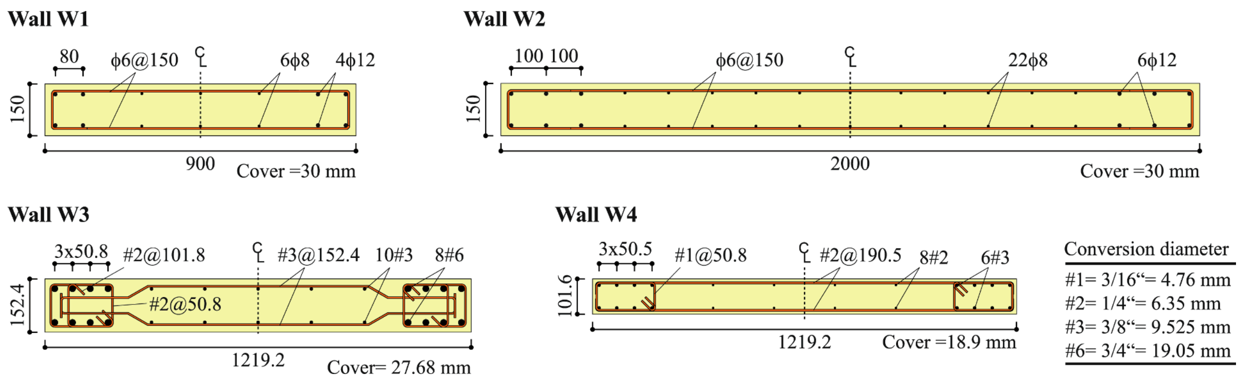

Fig. 5. Cross-section of experimental RC wall specimens: (a) W1; (b) W2; (c) W3; and (d) W4.

Table 2
Calibrated parameters for the stress-strain laws of the concrete model.

Specimen	E_c [GPa]	f_t [MPa]	f_c' [MPa]	G_c [N/mm]	G_t [N/mm]	K_s [–]	B^+ [–]	B^- [–]
W1	26.3	1.375	34.7	$1.75f_c'$	2.0	1.00	0.0	0.2
W2	38.5	1.023	41.7	$2.00f_c'$	2.0	1.00	0.0	0.2
W3	24.2	1.215	42.6	$1.75f_c'$	0.5	1.16	0.0	0.2
W4	21.0	0.001	34.5	$1.75f_c'$	2.0	1.13	0.0	0.2

Table 3
Calibrated parameters for the stress-strain laws of the steel model.

Specimen	Diameter [mm]	E_s [GPa]	f_y^+ [MPa]	f_y^- [MPa]	b^+ [–]	b^- [–]
W1	6	200	493.0	493.0	0.023	0.023
	8	200	513.0	513.0	0.023	0.023
	12	190	483.0	483.0	0.023	0.023
W2	6	210	518.9	518.9	0.018	0.018
	8	210	583.7	583.7	0.018	0.018
	12	210	576.0	576.0	0.018	0.018
W3	6.4 (#2)	200	308.7	308.7	0.018	0.018
	9.5 (#3)	200	398.7	398.7	0.018	0.018
	19.1 (#6)	200	429.3	429.3	0.018	0.018
W4	4.8 (#1)	200	390.6	520.8	0.025	0.035
	6.4 (#2)	200	403.2	537.6	0.025	0.035
	9.5 (#3)	200	390.6	520.8	0.025	0.035

strain relations consider the fracture energy FE-regularization to reduce the mesh-dependent results (see shaded area of Fig. 2); and a zero value of Poisson's modulus to achieve numerical convergence.

Originally, these uniaxial tensile/compressive stress-strain $\sigma^{\pm}(\varepsilon^{\pm})$ laws are piece-wise C^0-class functions, since their derivatives present a discontinuity at the boundary of each branch (e.g., peak and residual strength limits). It has been observed that these class of discontinuities generate numerical convergence problems for the solution of the concrete model, especially in strain-softening regimes. Therefore, to alleviate this problem, the tensile as the compressive uniaxial laws were converted locally to C^1-class functions. These modified functions consider the original stress laws and include three-order polynomials functions in a small region adjacent to each boundary of each branch ($0.05\varepsilon_o^{\pm}$). Details of this smoothing process is found elsewhere [58]. It is observed that the effect of this modification is negligible for the stress-strain response of the model, but improves their convergence considerably.

Fig. 2c shows an example of cyclic loading of the concrete model, where four important model characteristics are pointed out: **(i)** anisotropy, which accounts for the different tensile and compressive behavior; **(ii)** irreversible plastic/cracking strain; **(iii)** strain softening, which means that the modulus of elasticity decreases due to the irreversible damage process; and **(iv)** unilateral effect, which means that micro-cracks close under load reversals from tensile to compression showing partial stiffness recovery, whereas open cracks and stiffness degradation exists from compression to tensile load.

To define the confined concrete for the uniaxial compression stress-strain relation, two additional parameters are introduced (Fig. 3): the confined concrete peak strength $f_{cc}{}' = K_s f_c'$, and the strain at the peak strength $\varepsilon_{cc} = K_e \varepsilon_o^-$. The parameters $K_s, K_e \geqslant 1$ are determined using recommendations of Saatcioglu-Razvi [62], where the value of K_s depends on the amount and configuration of transverse reinforcement of the cross-section and K_e is given by $K_e = 1 + 5[K_s - 1]$.

Fig. 3 compares the uniaxial response of confined and unconfined concrete. The confined concrete has a higher maximum strength, and the peak occurs at a higher deformation (more ductile). However, in the post-peak response, the decay slope of the confined concrete is steeper

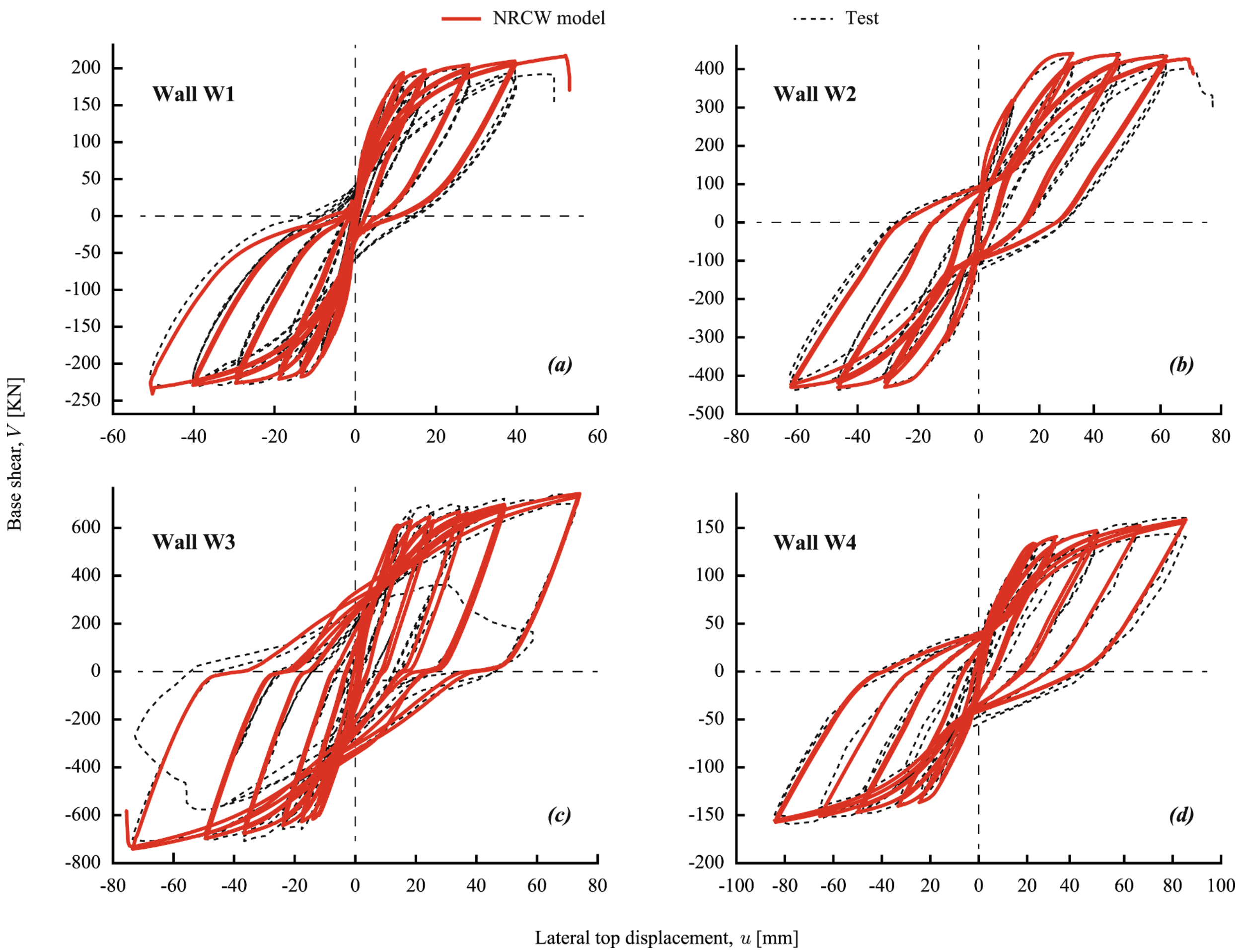

Fig. 6. Comparison between experimental and simulated load-deformation responses of the benchmark RC walls: (a) W1; (b) W2; (c) W3; and (d) W4.

Table 4
Response parameters of the RC wall FE models considered.

	K_y [kN/mm]			$V_{\max}$ [kN]			V_u [kN]			u_{max} [mm]			E_{dis} [kJ]		
Specimen	Test	FE	FE/Test	Test	FE	FE/Test	Test	FE	FE/Test	Test	FE	FE/Test	Test	FE	FE/Test
W1	44.1	45.0	1.020	214.0	224.0	1.045	192.0	210.0	1.094	49.3	52.6	1.067	65.0	58.0	0.892
W2	73.6	72.2	0.981	443.0	441.0	0.995	397.0	428.0	1.078	71.7	69.6	0.971	124.0	112.0	0.903
W3	52.3	60.3	1.152	740.0	743.0	1.004	736.0	711.0	0.966	74.1	75.0	1.013	344.0	396.0	1.151
W4	12.3	12.4	1.004	160.0	158.0	0.988	160.0	158.0	0.988	85.5	85.5	1.000	67.0	59.0	0.880

than the unconfined concrete response, which implies that the confined concrete is more brittle.

2.2.2. Steel

For steel rebars, the model defined by Menegotto-Pinto [54] was selected with the modification proposed by Filippou [64] to represent adequately the Bauschinger's effect. The asymmetric behavior associated with rebar buckling (in compression) and tension-stiffening (in tension) is implicitly included using a different tensile/compressive bilinear uniaxial stress law as shown in Fig. 4. Hence, the parameters for the model are the steel Young's modulus E_s; the tension/compression yield strength $f_y^{\pm}$, and the tensile/compressive hardening ratio $b^{\pm}$ ($b^{\pm} = E_p^{\pm}/E_s$ with $E_p^{\pm}$ as the tensile/compressive hardening modulus, respectively). The values proposed to model the Bauschinger's effect, and the cyclic degradation are those considered by Elmorsi et al. [65], i.e. R_0=20, Cr_1=18.5, and Cr_2=0.0015. The cyclic response of this model is shown in Fig. 4b.

2.2.3. Numerical implementation

The numerical integration of the material constitutive equations, necessary for both models, requires an algorithm to evaluate the updated stress tensor $\boldsymbol{\sigma}_{n+1}$, the internal state variables $\boldsymbol{\alpha}_{n+1}$, and the consistent tangent stiffness tensor $\frac{d\sigma_{n+1}}{d\varepsilon_{n+1}}$ at each integration point given a known strain increment $\Delta\boldsymbol{\varepsilon}$. On one hand, the updated stress algorithm of the concrete model is composed by the plastic and the damage component. For the plastic component, and due to the presence of the Heaviside function in the variable λ (Eq. 7b), an iterative algorithm is required to solve the updated effective stress tensor $\overline{\boldsymbol{\sigma}}_{n+1}$. This algorithm implies only four iterations and is faster than other complex implicit plastic algorithms. Conversely, the damage component is evaluated with an explicit scheme. A complete development of the numerical implementation of this model is explained elsewhere ([58]). On the other hand, the numerical implementation of the steel model is done by a well-known explicit scheme used to evaluate the updated uniaxial stress tensor σ_{n+1}.

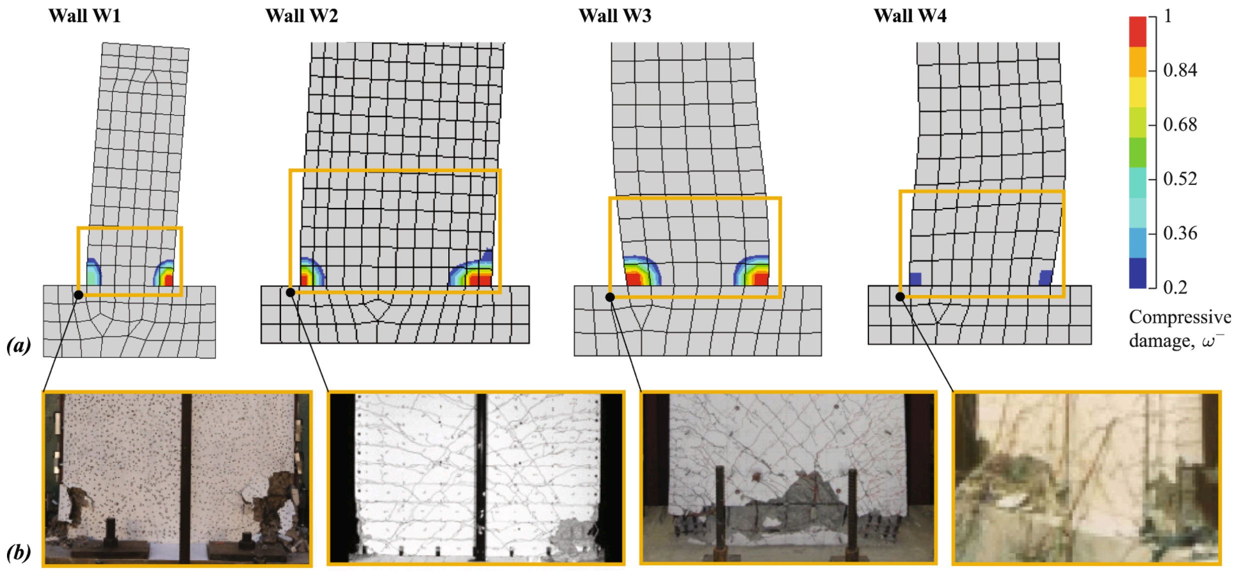

Fig. 7. Comparison between the experimental and predicted damage: (a) contour of compressive damage field ω^- of the FE model; and (b) experimental damage (Wall W1 [20], W2 [17], W3 [18] and W4 [24]).

Table 5
Values considered in the material parameters for the sensitivity analysis of RC wall FE models.

Material parameters	Reference	Value		
		min.	cen.	max.
Concrete				
Uniaxial tensile strength, f_t [MPa]	[48] [67]	$0.025f_c'$	$0.05f_c'$	$0.1f_c'$
Uniaxial compressive strength, f_c' [MPa]	Experimental test reports	$31.2^{(a)}$	$37.7^{(a)}$	$38.1^{(a)}$
		$36.8^{(b)}$ $46.6^{(c)}$ $34.5^{(d)}$	$40.9^{(b)}$ $48.6^{(c)}$ $40.8^{(d)}$	$45.0^{(b)}$ $51.3^{(c)}$ $45.7^{(d)}$
Tensile fracture energy, G_t [N/mm]	[67] and authors	0.5	1.0	2.0
Compressive fracture energy, G_c [N/mm]	[68] [31]	$1.5f_c'$	$1.75f_c'$	$2.0f_c'$
Tensile plasticity factor, B^+ [–]	[53] and authors	0.0	0.1	0.2
Compressive plasticity factor, B^- [–]	[53] and authors	0.1	0.2	0.3
Steel				
Tensile/compressive yield strength, $f_y^{\pm}$ [MPa]	Experimental test reports	$461^{(a)}$	$483^{(a)}$	$496^{(a)}$
		$505^{(b)}$ $453^{(c)}$ $399^{(d)}$	$519^{(b)}$ $477^{(c)}$ $434^{(d)}$	$533^{(b)}$ $501^{(c)}$ $456^{(d)}$
Tensile/compressive hardening ratio, $b^{\pm}$ [–]	Experimental test reports	1.0	3.0	5.0

$^{(a)}$, $^{(b)}$, $^{(c)}$, $^{(d)}$ for walls W1, W2, W3, W4, respectively.

3. Validation of the NRCW model

In this section, the experimental responses of four RC wall benchmark test specimens subjected to quasi-static cyclic loads are used to validate the NRCW model. The RC wall specimens were selected based on characteristics such as: geometry (slenderness), reinforcement ratio, boundary elements, and failure mechanism. They resemble typical Chilean RC walls (structures built previous the 2010 Chile earthquake), as appreciated by comparing Tables 1 and 6. The cross sections of each specimen are shown in Fig. 5, while their geometric properties and nominal Axial Load Ratios (ALR) η_w are shown in Table 1. ALR is defined as the ratio between the wall axial load N_w and section compression capacity, i.e., $\eta_w = N_w/A_g f_c'$, with A_g as the gross cross-section area of the wall, $A_g = h_w t_w$.

The four specimens were tested by different authors and can be classified into two groups: specimens with negligible amount of confinement, for which all concrete is considered unconfined (walls W1 and W2); and specimens with confined boundary elements (walls W3 and W4). Five response parameters are measured to evaluate the accuracy of the model and to calibrate the different material parameters: **(a)** initial lateral stiffness K_y; **(b)** peak base-shear force V_{max}; **(c)** maximum top lateral displacement u_{max}; **(d)** base-shear force V_u measured at u_{max}; and **(e)** dissipated energy under cyclic loading E_{dis}. The calibrated parameters for the uniaxial unconfined/confined compressive and tensile concrete laws are presented in Table 2, and the parameters for the uniaxial tensile/compressive steel laws with different bar diameters are presented in Table 3. Note that the difference in yield strength in tension and compression of steel for wall W4 is due to the tension stiffening effect [29,66].

Boundary conditions and loading patterns used for the analytical model were identical to the ones informed by the experimental test until reaching the failure of the wall. Axial load was applied by controlling force, and a horizontal cyclic displacement history was applied by controlling displacement, similar as it was done during the experimental tests. A mesh sensitivity analysis was performed for each wall model considering four different mesh sizes: 50, 100, 200, and 500 mm. Global and local responses considered for the different discretizations showed slight differences (mainly in u_{max}), being the model with a mesh size of 200 mm the one selected hereafter for the analyses presented next.

Fig. 6 shows the measured and simulated load-deformation responses for the four test specimens. It is apparent that for all cases, numerical results fit well the experimental response. Table 4 summarizes a comparison of the response parameters from the experimental and numerical models. Models of walls W1 and W2 predict an overstrength V_u of 9.4% and 7.8%, respectively. This is due to the fact that the concrete and steel models do not consider degradation for each cycle under a constant level of displacement. The same trend is present in the W3 wall model, where the effect is even more pronounced.

Shown in Fig. 7 is the experimental and predicted compressive damage field ω^- at the end of each test. For each wall, the model correctly predicts the location of damage in the specimens, usually at the bottom edges of the walls. The gray shaded area in each wall represents

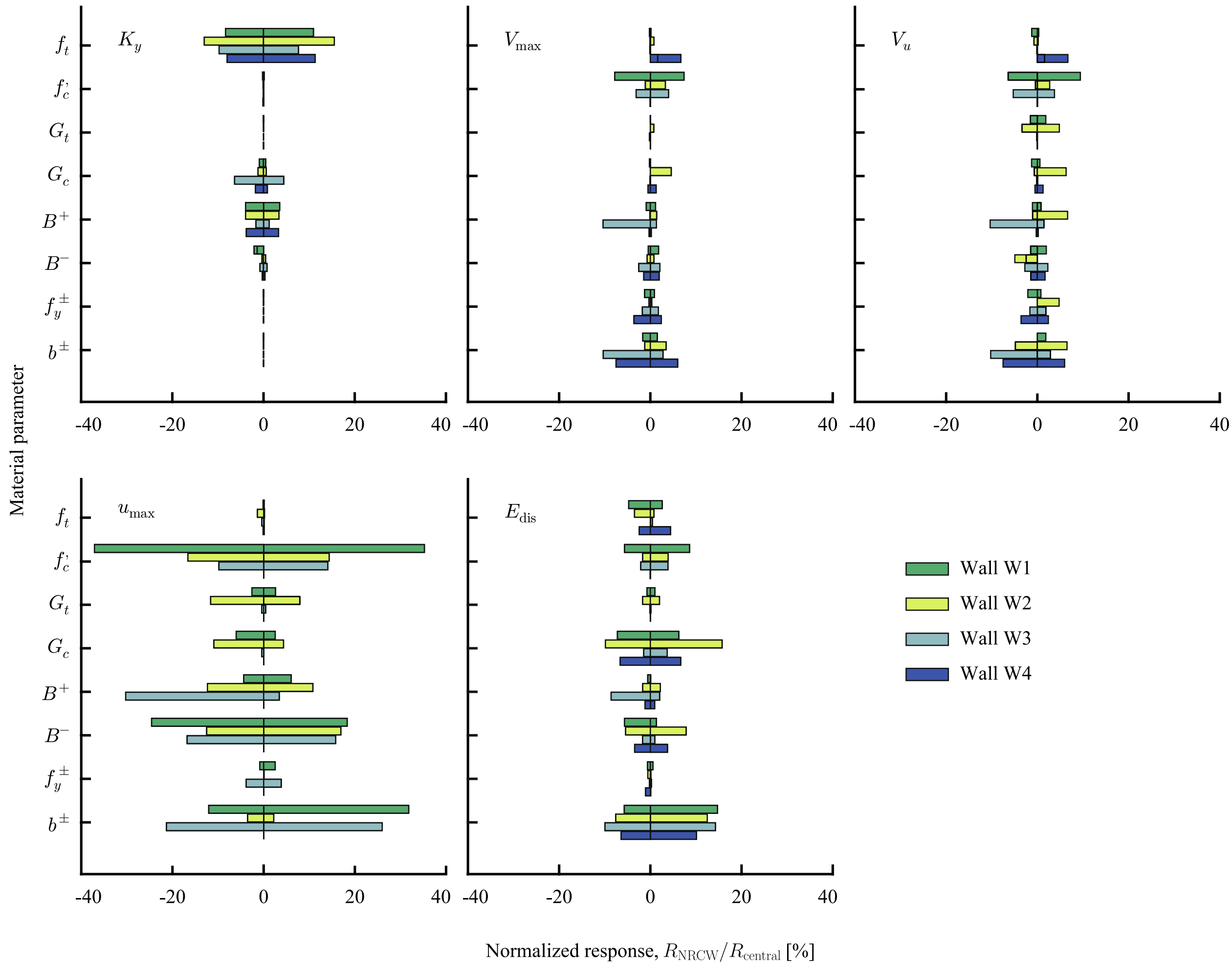

Fig. 8. *Percentual variability in wall responses produced by changes in material parameter values relative to the case with central values.*

the undamaged area, while the colored area represents different levels of damage. The regions shaded with blue-to-red colors have all lost their concrete cover, the regions with yellow and orange colors represent partial crushing of concrete, whereas the red areas represent zones with completely concrete crushing. For walls W1, W2 and W4, damage is localized mainly at the bottom edges, where failure occurs at one side due to concrete crushing and there is agreement with the corresponding numerical models. However, the observed experimental failure of wall W3 involved concrete crushing at both bottom edges of the wall section with spalling of the concrete cover that extended across the complete section. While in the numerical model, damage agrees in the vertical location, it does not cross the complete section. Extension of damage also varies for each wall. The total height of the damage zone in wall W1 is 30 cm, while the width is about 20 cm at the right side and 15 cm at

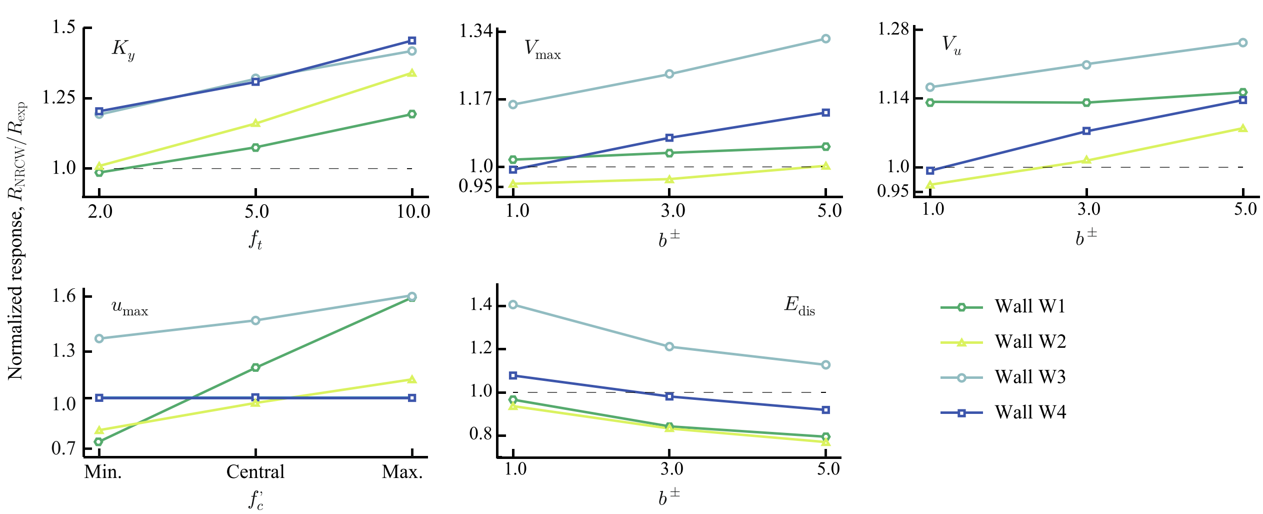

Fig. 9. Normalized response versus the most critical material parameters.

the left. For W2, the damaged zone is 40 cm high, and 45 cm and 27 cm wide at the right and left bottom edges of the wall respectively. In the case of wall W3, the height and width of the zone is about 30 cm at both wall edges. The extension of the damaged zone in wall W4 is around 10 cm in height and wide at the bottom edges of the wall. The damaged width of the wall l_d is larger than the confined length of the edges and equal to 20% of the wall length l_w, and about 10% the wall height; the damaged height h_d varies between 10% and 15% of the wall height, i.e. $l_d \approx 0.20 l_w \approx 0.10 h_w$ and $h_d \approx (0.10 - 0.15) h_w$. Wall W4 is not used in these estimates since it did not present completely crushed concrete.

4. Sensitivity analysis with the NRCW model

From the results of the numerous simulations runs during model calibration of material parameters of the RC wall specimens, it became apparent that in the NRCW model, some material parameters are more critical than others in reproducing the actual response of the RC walls. Because the value of each material parameter is not completely deterministic, it has to be calibrated to provide an accurate representation of the cyclic response of the walls.

To study the effect of each material parameter, models for the four benchmark tests were run with different values of the material parameters. The material parameters for the concrete model were: the uniaxial tensile strength f_t (normalized by the uniaxial compressive strength); the uniaxial compressive strength $f_c^{'}$; tensile fracture energy G_t; compressive fracture energy G_c; and the tensile/compressive plasticity factors $B^{\pm}$.

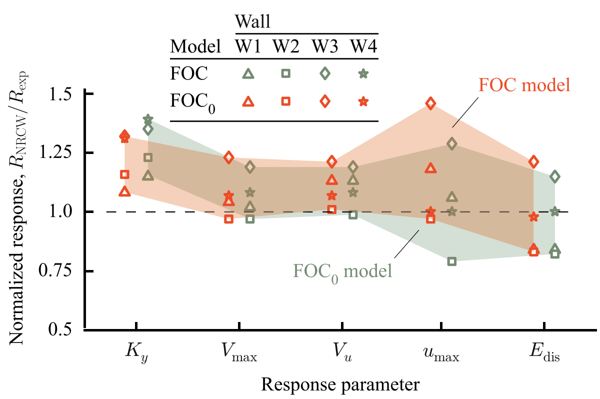

Fig. 10. Wall response comparisons as a function of the plastic component of concrete.

Furthermore, the material parameters for steel were: the tensile/compressive yield strength $f_y^{\pm}$; and the tensile/compressive hardening ratio $b^{\pm}$. The nominal Young's modulus for concrete E_c was estimated by the ACI equation [48] (i.e., $E_c = 4700\sqrt{f_c^{'}}$ in MPa) for normal weight concrete, and the steel modulus E_s was taken from test results since no significant variability was observed. The residual strength of concrete was also considered as a variable; however, for values between 0 and $0.2f_c^{'}$ it did not show any significant variation for the wall response.

Three different values were considered for each parameter and wall, which were selected according to suggestions of different researchers, codes, guidelines, and by the authors judgment. Table 5 summarizes the values considered in the sensitivity analysis for all material parameters.

Fig. 8 summarizes the results of the sensitivity analysis. All numerical response parameters were normalized with respect to the central value of the corresponding parameter. Results show that u_{max} is the most sensitive response parameter, while the maximum and ultimate base-shear (V_{max} and V_u) are the least sensitive. The uniaxial tensile strength of concrete f_t produces the largest variation in the initial stiffness K_y of walls, which reaches a maximum value of 16% in wall W2, whereas the parameters G_c,$b^{\pm}$,$f_y^{\pm}$, and $f_c^{'}$ produce a negligible effect. The tensile/compressive hardening ratio of steel $b^{\pm}$ generates the largest variation in the peak base-shear V_{max}, showing a peak value of 10% in wall W3, while the fracture energy in tension G_t generates no variation in this response. The maximum top lateral displacement u_{max}, is strongly influenced by $f_c^{'}$, which is reflected by a peak variation of 37% for wall W1; the value of f_t does not influence u_{max}. In the case of ultimate base-shear V_u, results show that $f_c^{'}$ and $b^{\pm}$ leads to a variation of up to 10%, and that V_u is not sensitive to f_t. Finally, the energy dissipated E_{dis} is more influenced by $b^{\pm}$ than by any other parameter with a peak variation of 15% in wall W3; $f_c^{'}$ is the parameter with lowest effect.

Fig. 9 shows the variation of each wall response parameter as a function of the most critical material parameter identified. The values of the numerical models have been normalized by the experimental response values. It is observed that the normalized initial stiffness K_y increases almost linearly as f_t increases, and also do the normalized peak base shears V_{max}, and V_u as $b^{\pm}$ increases. The variation is clearly larger for walls with confined boundary elements (W3 and W4) due to the higher vertical steel ratio at the boundaries. For the maximum top lateral displacement u_{max}, the value usually increases with the value of $f_c^{'}$ for walls W1-W3, but differences in the rate of increase are quite significant. Furthermore, the value of V_u also increases as the parameter $b^{\pm}$

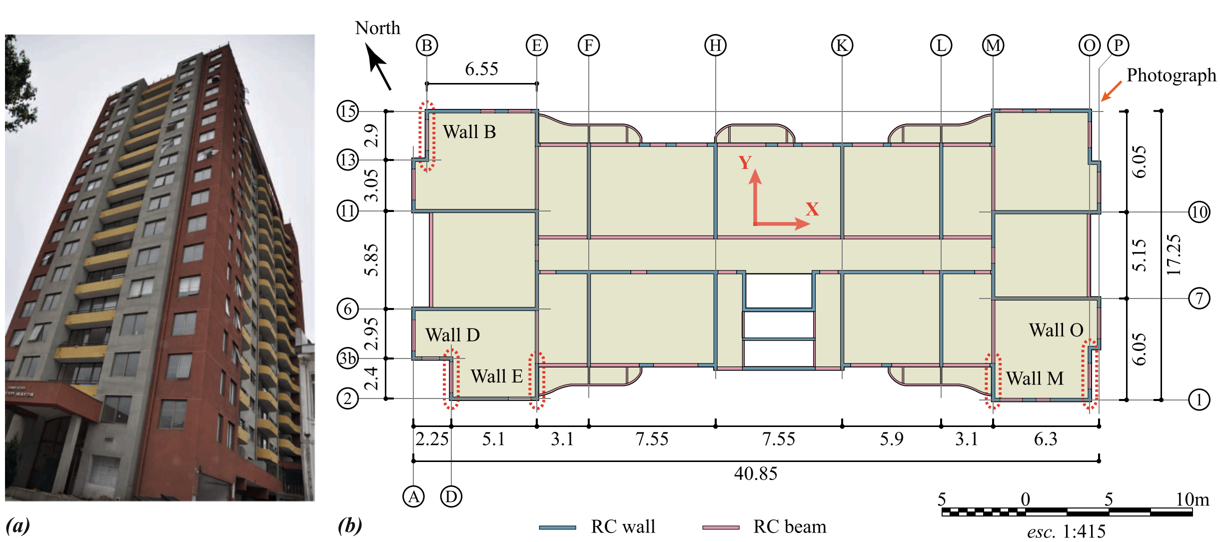

Fig. 11. CM building: (a) photograph; and (b) structural plan of a typical story (all units in meters).

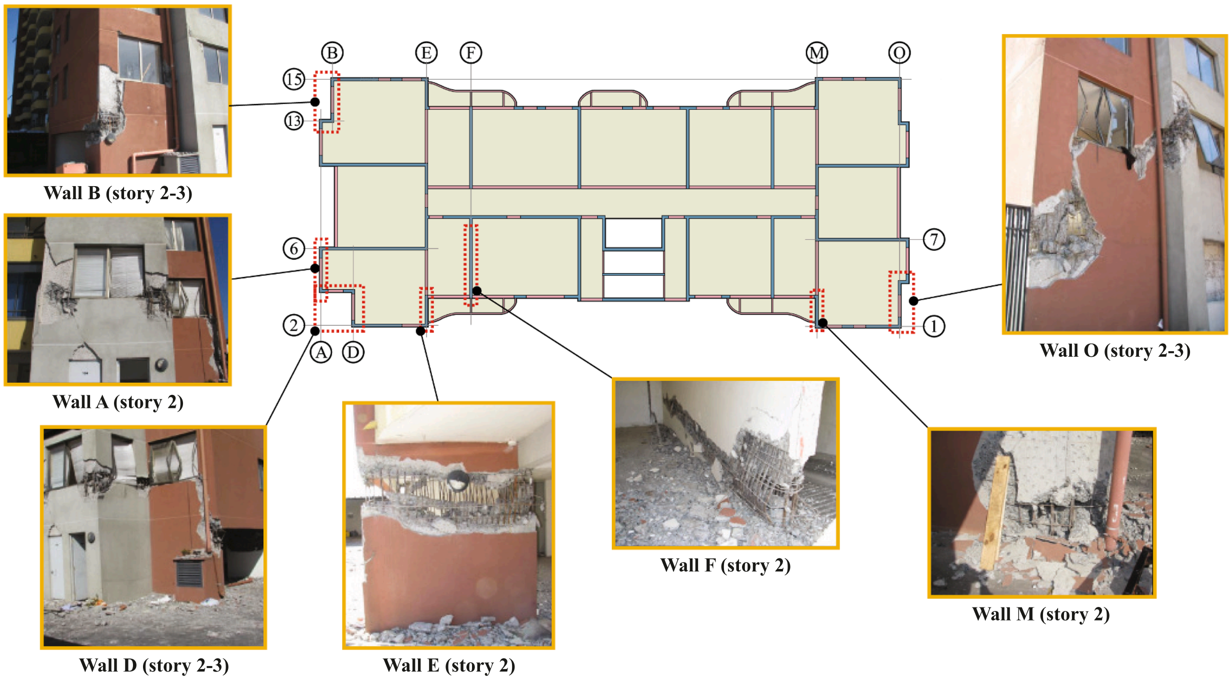

Fig. 12. Observed damage in RC walls of the CM building after 2010 Chile earthquake (courtesy of Westenenk et al. [13]).

increases, while the energy dissipated E_{dis} by the walls decreases as the value of $b^{\pm}$ increases.

The influence on the wall response of the plastic component of the concrete model was also studied. Two cases were considered: (i) concrete model with plastic strains, i.e. non-zero plastic factors $B^{\pm} > 0$ (denoted as FOC model hereafter); and (ii) concrete model without plastic strain, $B^{\pm}=0$ (denoted FOC_0 hereafter). All other material parameters are left constant. Note that the FOC concrete model is the same that is used in the NRCW model and the values of the $B^{\pm}$ factors for each wall are given in Table 2.

Shown in Fig. 10 is the comparison between the normalized results for both concrete models. In general, dispersion of the results ranges between −25% and +50%, which is quite significant. Results tend to be slightly better for the case of FOC with the exception of K_y for which FOC shows a slight bias to overestimate the value.

5. Case study: Centro Mayor (CM) building

This section presents a case study of a real RC wall building that suffered severe structural damage during the 2010 Chile earthquake in the city of Concepción. The NRCW model just presented was used to simulate the seismic performance of the building, and the damage location and distribution.

5.1. Building characteristics and observed damage pattern

The CM building was located in Concepcion, Chile, and was built in 2005 for residential use. It had 18 stories and one basement, and the plan resembles that of a fish-bone [6], which is typical of these residential structures in Chile. According to the post earthquake structural report of the building, it was founded on unsaturated gravel and clay soil characterized by a shear wave velocity V_{s30} less than 400 m/s (soil type III according to the Chilean seismic code NCh433 [69]). The building was designed considering a uniaxial compressive strength of concrete $f_c^{\prime}$ of 25 MPa, and steel rebars with 420 and 630 MPa nominal yield and ultimate strength, respectively. The building structure consisted of RC walls of 20 cm of thickness, beams with different heights, and 15 cm thick floor slabs. A photograph of the building and a typical story floor plan (stories 2–16) are presented in Fig. 11.

The observed damage in some walls of the building after the 2010 Chile earthquake is shown in Fig. 12. It is apparent that damage tends to occur in walls located in the transverse direction at three of the four building corners. In axes F and M, concrete crushing and buckling of vertical reinforcement due to bending and compression is evident. In walls located in axes A and E, the lack of confinement is evident by looking at the wall crack that propagated throughout the complete section of the wall. This is indicative of the role that the (high) axial load played in its failure. Furthermore, a multistory damage pattern was observed in three of the four corners of the building. In this case, failure started at a discontinuity and propagated throughout the wall up to the window opening in the adjacent story. Similar failure mechanisms as seen for this building were observed in several others buildings [5,6]. Walls B, D, E, and M, from the base of the second-story to fourth-story (2.95–8.15 m in height) presented the most damaged sections. These walls are referred hereafter as critical walls, whose geometrical properties and reinforcements are reproduced in Table 6.

After the earthquake, the laboratory of the Scientific and Technological Research Unit of the School of Engineering at Universidad Católica (DICTUC) tested specimens of the different materials of the building [70]. Concrete specimens and steel rebars of different diameters (from 8 to 25 mm) from walls and slabs of all stories were

Table 6
General characteristics of critical walls of the CM building at second story: h_w is the clear story height; l_w is the horizontal length of the wall; t_w is the thickness of the wall segment; ρ_v is the vertical reinforcement ratio; ρ_h is the horizontal reinforcement ratio; and ρ_b is the volumetric reinforcement ratio of the confined boundary elements

Wall	l_w [cm]	h_w [cm]	t_w [cm]	h_w/l_w [–]	ρ_v [%]	ρ_h [%]	ρ_b [%]
Wall B	310	360	20	1.16	1.40	0.34	2.53
Wall D	260	360	20	1.38	0.84	0.25	2.44
Wall E	220	360	20	1.67	2.09	0.39	1.71
Wall M	228	360	20	1.58	0.85	0.25	1.42

Table 7
Measured concrete parameters for the CM building model.

Element	Story	$E_c^{(a)}$ [GPa]	$f_t^{(b)}$ [MPa]	f_c' [MPa]	G_t [N/mm]	$G_c^{(c)}$ [N/mm]	K_s [–]	B^+ [–]	B^- [–]
Walls	−1	36.3	–	59.7	–	–	–	–	–
	1	36.0	5.9	58.8	2.0	117.6	1.25	0.0	0.2
	2	33.9	5.2	52.0	2.0	104.0	1.25	0.0	0.2
	3	32.7	4.8	48.3	2.0	96.6	1.25	0.0	0.2
	4	30.7	4.3	42.7	2.0	85.4	1.25	0.0	0.2
	5–18	30.4	–	41.8	–	–	–	–	–
Slabs	–	34.0	–	52.4	–	–	–	–	–

(a) $E_c = 4700\sqrt{f_c'}$ in MPa; (b) $f_t = f_c'/10$; and (c) $G_c = 2.0 f_c'$

sampled to determine the as-built material properties. Table 7 and 8 show the uniaxial compressive strength of concrete f_c' for all stories, the yield stress f_y and the ultimate strength f_u of steel rebars for each diameter, respectively. In the case of concrete, test results showed large variability for the lower 5-stories (basement and first four stories) and f_c' values decreasing in height. For stories 5 through 18, f_c' values vary around 41.8 MPa. For the case of steel, yield stress decreases as bar diameter increases, while the ultimate stress is rather constant. Despite the fact that the steel model is capable of implicitly considering bar buckling, it was neglected since it only occurs in the region of concrete crushing; previous research work has shown that concrete crushing triggers the collapse of the walls [13,9–12]. Moreover, previous research results that consider bar buckling showed that the effect was not significant in the walls [26].

5.2. Non-linear building model

Three different FE models of the structure were developed: (i) a linear-elastic model using ETABS software [71], which is denoted hereafter as ET_o; (ii) a linear-elastic model using ANSYS software [52] named AP_o; and (iii) a non-linear model using ANSYS named AP.

The linear-elastic ET_o and AP_o models consider the following assumptions: **(1)** the 3D models include all structural elements; **(2)** all frame and shell elements were defined with a Young's modulus of 23.413 GPa and a mass density ρ_c of 2.50 ton/m^3; **(3)** a gross inertia EI_g was assumed for all structural elements; **(4)** in-plane rigid diaphragm was assumed for slabs; **(5)** models were fixed to the base at ground level; **(6)** seismic mass equal to the self-weight (structural and nonstructural elements) plus 25% of the life loads, as specified by the Chilean code [69]; and **(7)** a compatible mesh between all structural elements was generated with a maximum element size of 500 mm.

The inelastic AP model considers the following modeling assumptions: **(1)** all structural elements of the superstructure and basement were included; **(2)** RC beams and columns were modeled using 2-node frame elements (BEAM188) with six DOFs per node and the Timoshenko formulation [52]; **(3)** walls and slabs were simulated with 4-node (or 3-node) layered-shell elements (SHELL181) for concrete, and the uniaxial smeared-reinforcement elements (REINF265) for steel rebars; **(4)** all beams, slabs, walls at the basement, and all elements of stories 5–18 were considered to have elastic behavior, while the walls in stories 1–4 were modeled using the NRCW model previously presented in Section 2; **(5)** in-plane rigid diaphragms are assumed for the slabs; **(6)** the structure is fixed to the base at the bottom of the basement level; **(7)** seismic mass is included as for the AP_o model; **(8)** for the elastic walls and slabs, reduction factors of 0.7 and 0.25 were considered for the gross stiffness (EI_g), respectively (as recommended by ACI [48]); and **(9)** a compatible mesh was automatically generated with a maximum mesh size of 500 mm (average mesh size of 400 mm) for all elements.

Table 8
Measured steel parameters for the CM building model.

Diameter [mm]	$E_s^{(a)}$ [GPa]	$f_y^{\pm}$ [MPa]	f_u [MPa]	$b^{\pm}$ [–]
8	200	606	772	0.03
10	200	583	781	0.03
16	200	537	767	0.03
22	200	470	711	0.03
25	200	473	755	0.03

(a) values based on to ACI-318–19 [48].

The material parameters used in the model were those shown in Tables 7 and 8, which are based on the test specimens and numerical results of Sections 3 and 4. The value of E_c was calculated using the ACI's expression for normal weight concrete, i.e., $E_c = 4700\sqrt{f_c'}$ (MPa) [48], whereas the Young's modulus of steel E_s was assumed as 200 GPa (as recommended by ACI [48]).

The AP model was defined with a total number of 130474 nodes and 162687 elements, of which 6031 correspond to BEAM188, 130369 to SHELL181, and 26287 to REINF265 elements. A 3D view of the meshed model, a slice of the building for the second and third stories, and some critical walls are shown in Fig. 13 (the other 2 models had the same number of nodes, shell, and beam elements).

An elastic modal analysis was initially run for the three models to check their geometry, mass and stiffness distributions and to compare their dynamic properties. Table 9 shows a comparison of the first nine periods of vibration of the building obtained with the ETABS and ANSYS models. Vibration periods are slightly different between models, with differences that range between 0.48% and 6.2%, which are in agreement with the epistemic uncertainty results of Chacón et al. [39]. In general, and for all modes, the periods of the AP_0 models are larger than for the ET_0 ones, which can be attributed to differences in their FE formulations since the masses are essentially the same.

5.3. Non-linear response-history analysis

The non-linear AP model was subjected first to a static analysis with gravitational loads followed by a NRH analysis. The three components of the ground motion recorded at the station "Concepción centro" of the 2010 Chile earthquake were applied to the model. The ground motion was recorded at the nearest station from the building (670 m distance, Fig. 14) and in a similar soil type. Shear wave velocity V_{s30} of 223 m/s has been estimated for the soil (soil type III according to Chilean seismic code [69]). Because of computational storage limitations, only the first 75 s of the ground motion record were considered in the analysis, which cover well the high intensity part of the ground motion.

Fig. 15 shows the three components of the selected record (i.e. E-W, N-S and Z-directions) and their response spectrum corresponding to a critical damping ratio of 5%. The figure also shows the 5% damping design response spectrum of the Chilean code (NCh433 [69]) with a reduction factor R_0 of 1 (elastic) and 11 (for RC walls). For the fundamental period region of the building, the peak ground acceleration in the E-W direction is considerably smaller than in the N-S direction; despite this and as already described, damage in the building was localized in the Y-direction (weak direction), which is oriented in the E-W direction

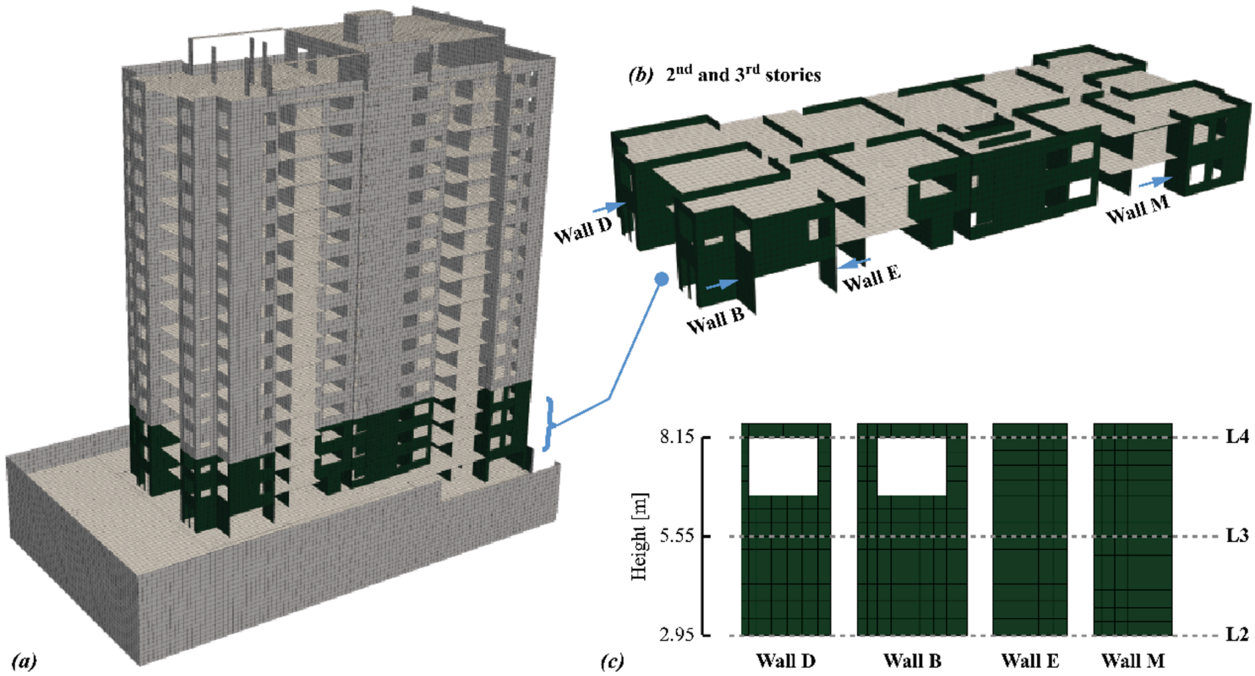

Fig. 13. FE model of the CM building: (a) 3D view; (b) slice of the building for the second and third stories; and (c) elevation of walls at the critical zone in the lower stories.

Table 9
Comparison of vibration periods for the first 9 modes of the CM building models.

Model	Period [s]								
	T_1	T_2	T_3	T_4	T_5	T_6	T_7	T_8	T_9
ET_0	0.813 (Y)	0.691 (X)	0.570 (Θ)	0.205	0.191	0.187	0.186	0.162	0.158
AP_0	0.847 (Y)	0.723 (X)	0.573 Θ)	0.212	0.197	0.195	0.176	0.169	0.168
AP	0.764 (Y)	0.644 (X)	0.515 (Θ)	0.314	0.269	0.251	0.218	0.215	0.208

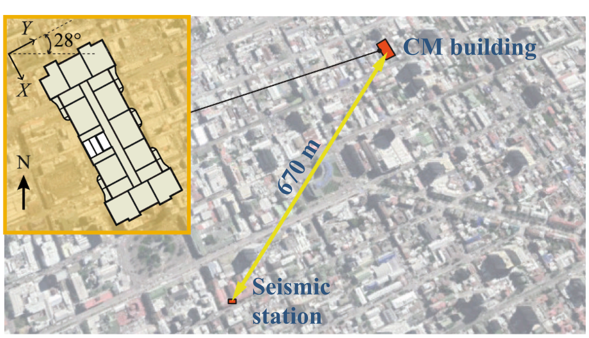

Fig. 14. CM building location.

(Fig. 14). Also notice that both response spectra are considerably higher than the reduced design spectrum ($R_o = 11$).

The NRH analysis in ANSYS considered the following options: (i) a transient full dynamic analysis; (ii) Newmark's time integration method with numerical damping μ, where the second-order integration parameters β and γ are defined as $\beta = (1+\mu)^2/4$ and $\gamma = 1/2 + \mu$, and a default value of μ=0.005 for high speed simulations, which leads to β=0.2525 and γ=0.5050; (iii) the Newton–Raphson method to solve the nonlinear equations associated with the consistent tangent stiffness tensor of the inelastic material models; (iv) an integration time step of 0.005 s, which is automatically reduced in critical loading cycles due to convergence problems; and (v) a Rayleigh's damping model [72] defined by

$$\underline{\boldsymbol{C}} = a_0\underline{\boldsymbol{M}} + a_1\underline{\boldsymbol{K}} \text{ with} \tag{11a}$$

$$a_0 = \frac{2\zeta_o\omega_a\omega_b}{\omega_a+\omega_b} = \frac{4\pi\zeta_o}{T_a+T_b} \text{ and} \tag{11b}$$

$$a_1 = \frac{2\zeta_o}{\omega_a+\omega_b} = \frac{\zeta_o T_a T_b}{\pi(T_a+T_b)} \tag{11c}$$

where a_0 and a_1 are the mass and stiffness proportional factors, respectively; and $\omega_a = 2\pi/T_a$ and $\omega_b = 2\pi/T_b$ are the circular frequencies associated with the pair set of pre-selected target periods $\{T_a, T_b\}$ to impose damping ratio ζ_o. In this analysis, a target critical damping ratio ζ_o=3% was chosen for the periods $\{0.2T_1, 1.5T_1\}$ [49].

For the sake of simplicity, three response parameters were monitored: **(i)** the maximum lateral story drift $\delta_{\max}$, which is defined as $\delta_{\max} = \max_t[\Delta_u(t)/h]$, where $\Delta_u(t)$ is the relative inter-story displacement in the direction of analysis measured at the center of mass of each floor and h is the inter-story height; **(ii)** the ALR in time $\eta(t)$ (response-history) and its maximum value $\eta_{\max} = \max_t[\eta(t)]$ for the critical walls (B, D, E, and M) measured at 2.95 m height (i.e., in the critical section where the building suffered larger damage); and **(iii)** the evolution of the compressive damage field $\omega^-(t)$ for critical walls between the base of the second and the fourth-stories (from 2.95 to 8.15 m).

Fig. 16a shows the maximum interstory drift $\delta_{\max}$ and the response history of ALR $\eta(t)$ for the critical walls. It is observed that the largest

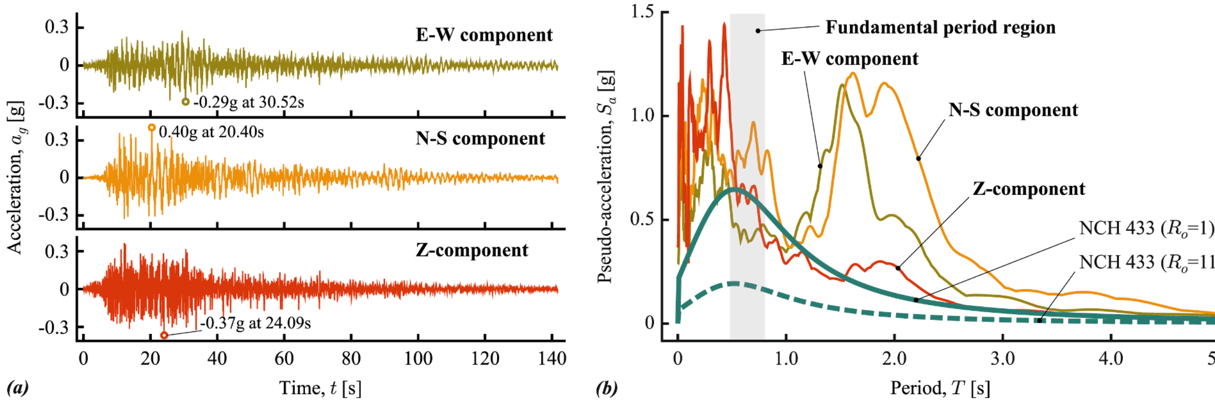

Fig. 15. Ground motion record considered in the NRH analysis of CM building: (a) acceleration records; and (b) response spectrum of the ground motion and comparison with the design spectrum of NCh433 code [69] for the same soil.

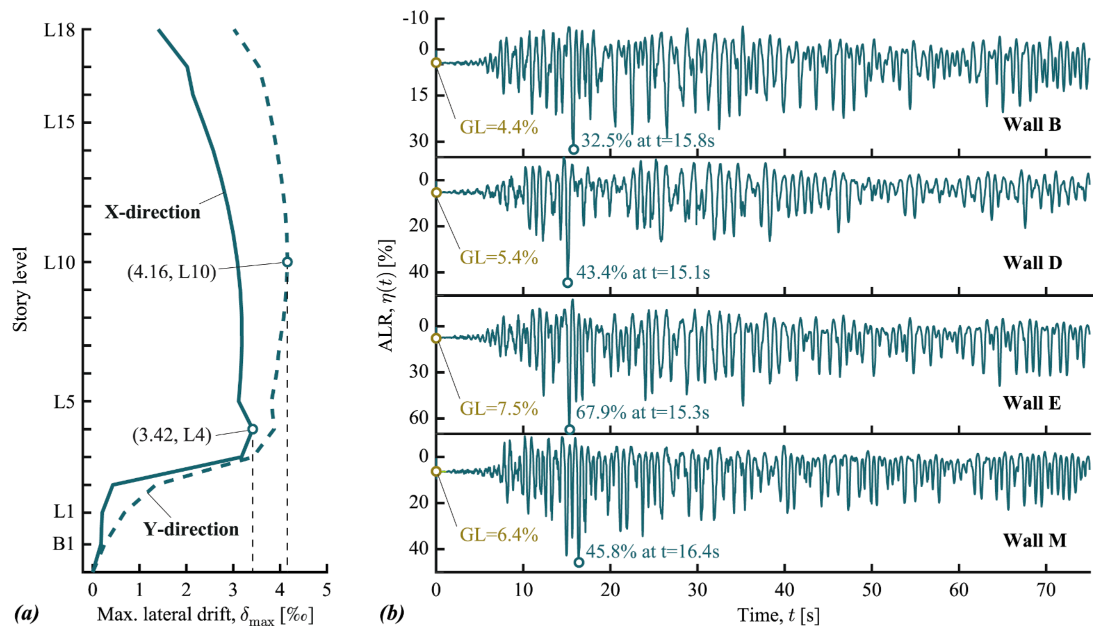

Fig. 16. Non-linear response parameters of CM building model: (a) maximum story drift, $\delta_{\max}$; and (b) response history of ALR $\eta(t)$ for the critical walls.

drift of the structure occurs in the Y-direction, reaching a peak of about 4.16‰, while 3.42‰ is obtained in the X-direction. For the second story, strong localized damage occurs causing a slight inclination of the building, which induces rigid body rotations in the upper stories. Coincident with earlier findings [42], the ALR increases significantly as result of the dynamic behavior of the building (see Fig. 16b). For instance, ALR in wall E is 7.5% due to gravitational loads; whereas during the earthquake, this parameter reaches up to at 67.9% caused by significant load transfer primarily through the slabs and the interaction with other walls. Slabs were checked and they remain elastic in such condition [56].

The compressive damage field ω^{-} in the critical walls of the building is summarized in Fig. 17. Comparing Figs. 17 and 12, it is apparent that the numerical model reproduces correctly the damage observed in the structure after the earthquake. The model localizes the damage in the same walls and captures successfully the multistory damage observed in the building corners, which starts in the vertical irregularities and propagates up to the corner of the window in the contiguous story.

Fig. 18 shows the ALR history $\eta(t)$ of wall O and its damage field in compression ω^{-} at different instants of the response. In the first 14 s of the earthquake record, before ALR reaches its peak value, damage is negligible ($\omega^{-}_{max} \approx 0$). Then, at the instant of peak value for ALR (16.7 s), damage in the wall increases sharply and becomes evident ($\omega^{-}_{max} \approx 0.54$), keeping a constant damage level until the end of the response. This proves that the failure of these RC walls is brittle.

6. Sensitivity analysis of building response

This section studies the sensitivity of the inelastic response of the building as a result of three different modeling assumptions: the parameters in the Rayleigh's damping model; the effective bending stiffness of the linear-elastic elements; and the incorporation (or not) of the vertical component of ground motion.

6.1. Effect of Rayleigh's damping model

To analyze the effect of damping in the building, two parameters in the Rayleigh's damping model were varied: target critical damping ratio ζ_o, using 3% and 4%; and the set of pre-selected periods $\{T_a, T_b\}$, using $\mathscr{T}_1 = \{0.2T_1, 1.5T_1\}$ and $\mathscr{T}_2 = \{T_1, T_3\}$. Therefore, combining both cases, four models were considered M1, M2, M3, and M4, which are listed in Table 10.

Fig. 19 shows the critical damping ratio ζ as a function of the frequency $f = 1/T$ using the two sets of pre-selected periods ($\mathscr{T}_1$ and $\mathscr{T}_2$)

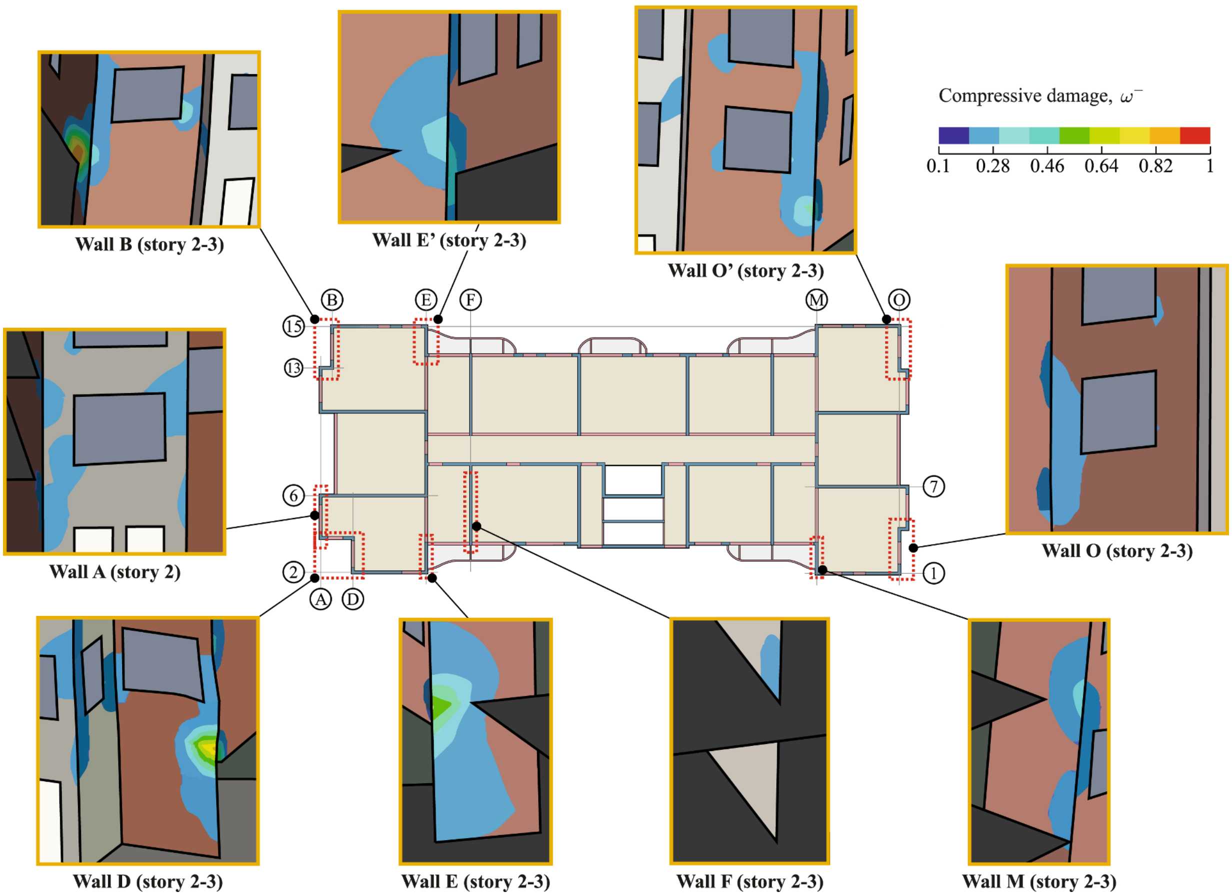

Fig. 17. Compressive damage field ω^- for the critical walls of the building model at the end step.

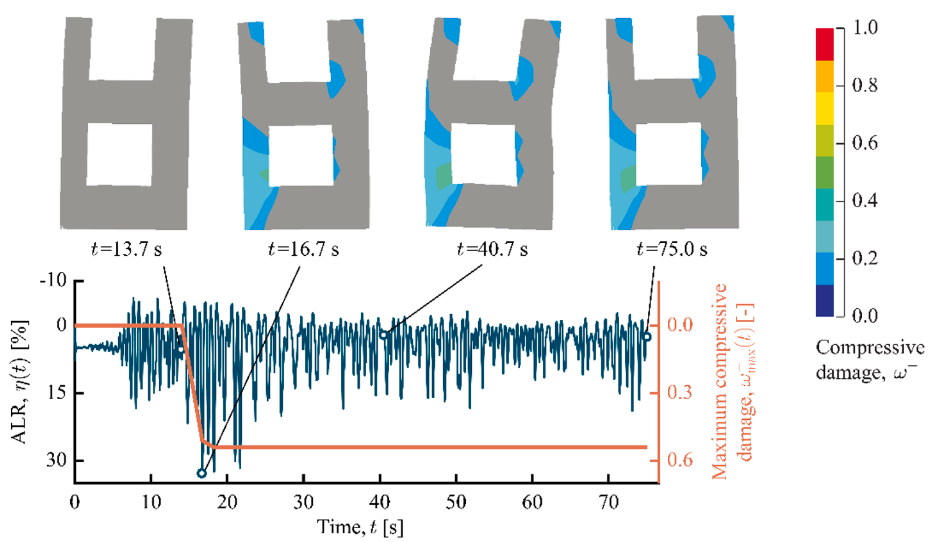

Fig. 18. History of the ALR $\eta(t)$ in wall O at the critical section and their compressive damage field ω^- at different times.

for this building. It also includes the first nine fundamental periods of vibration of the building model. It is observed that the pair $\mathscr{T}_1$ underestimates the ζ_o value for the first and second modes of vibration, while the third is close to the target value ζ_o. Conversely, $\mathscr{T}_2$ provides a critical damping ratio for the second mode closer to ζ_o. For the higher modes of vibration, both models estimate values of ζ larger that ζ_o. The pair $\mathscr{T}_1$ provides in this case values higher than the pair $\mathscr{T}_2$.

Fig. 20a shows the maximum lateral story drift δ_{max} using different values in the parameters of the Rayleigh's damping model. Inter-story drifts in the X-direction tend to be more sensitive to this variation than in the Y-direction. Moreover, the inter-story drift values using the set $\mathscr{T}_1$ (M1 and M2 models) are higher than those of the set $\mathscr{T}_2$ (M3 and M4 models) in both directions, showing the effect of the smaller values of critical damping ratio ζ for the first and second modes of vibration (Fig. 19). Moreover, an increase in the target critical damping ratio ζ_o (M2 and M4 models) leads to a decrease in the drift values, which is

Table 10
Cases for the sensitivity NRH analysis of CM building model.

Model	Rayleigh's damping parameters		Gross stiffness reduction factor	
	ζ_o[%]	T_a, T_b	Walls	Slabs
M1	3.0	$0.2T_1$,$1.5T_1$	1.0	1.0
M2	4.0	$0.2T_1$,$1.5T_1$	1.0	1.0
M3	3.0	T_1, T_3	1.0	1.0
M4	4.0	T_1, T_3	1.0	1.0
M5	3.0	$0.2T_1$,$1.5T_1$	0.7	1.0
M6	3.0	$0.2T_1$,$1.5T_1$	0.7	0.25

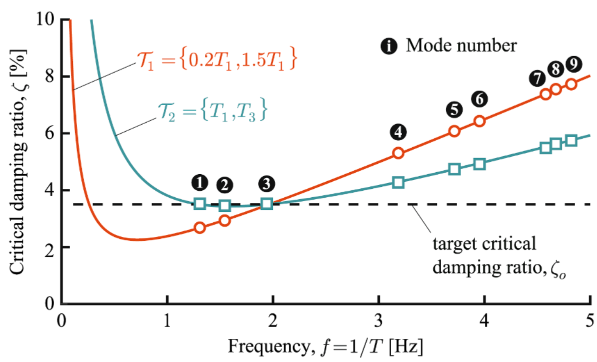

Fig. 19. Critical damping ratio ζ as function of the frequency f using two pair set of pre-selected periods $\{T_a, T_b\}$ for the CM model. Both curves were calibrated with a target critical damping ratio ζ_o of 3.5%.

more significant in the X-direction, with a maximum relative decrease of 15% for M1 respect to the M3 model at the fourth-story.

Fig. 21a and Table 11 show the response history ALR $\eta(t)$ of the four critical walls and their respective peak values $\eta_{\max}$ due to the variation in the Rayleigh's damping model parameters. Furthermore, Fig. 21b shows the compressive damage field ω^- at the critical walls. Results show that an increase in the target critical damping ratio ζ_o (M2 and M4) reduces the values of the compressive damage and their damage zone in all walls relative to the M1 and M3 models, as well as the value of $\eta_{\max}$. Moreover, the instant at which the peak of ALR occurs also changes, and hence, the sequence in which each wall fails too. Hence, M1 and M3 models present higher values of ALR relative to M2 and M4 models, with a difference of 2.5%. Moreover, ALR also increases in wall sections with openings.

6.2. Effect of the effective bending stiffness

Codes suggest different values for the reduction factors of the gross stiffness EI_g for an elastic analysis model. Values depend on the type of element and characteristics of the section to account for different levels of cracking. ACI 318 [48] suggests a value of 0.70 for uncracked walls and 0.25 for slabs; ASCE/SEI 41 [46] only specifies values for cracked walls; and FEMA P-1050–1 [47] suggests to analyze the structure considering an upper- and lower-bound effective stiffness for diaphragms. Based on this, the response of the structure was analyzed considering two cases in order to compare with the AP base model: (i) reduction factors for gross stiffness EI_g of 0.70 for walls and 1.00 for slabs (M5 model); and (ii) reduction factors for gross stiffness EI_g of 0.70 for walls and 0.25 for slabs (M6 model). Table 10 lists details of both models.

Shown in Fig. 20b is a comparison of the maximum lateral interstory drift $\delta_{\max}$ of the building for different effective stiffness values (models M1, M5, and M6). Results show that a reduction of 30% in the bending stiffness of walls does not change the peak story drift values significantly. Indeed, increases are only 0.16‰ and 0.03‰ in the X- and Y-directions, respectively, relative to the M1 model. However, as the bending slab stiffness decreases to 25%, the story drifts increase more than 100% relative to the M1 model, reaching values of 3.42‰ and 4.16‰ in the X- and Y-directions, respectively. This confirms again the importance of the slab behavior in this type of wall structures; the same phenomena has been observed in other building types [39].

Fig. 22 and Table 12 show the ALR history $\eta(t)$ of the four critical walls and their respective peak values $\eta_{\max}$ due to variation in the effective bending stiffness values for the building model (models M1, M5 and M6). Also, Fig. 22b shows the compressive damage field ω^- in the critical walls. It is observed that ALR in the M4 model changes slightly relative to the M1 model. Walls E and M show an increase in their ALR,

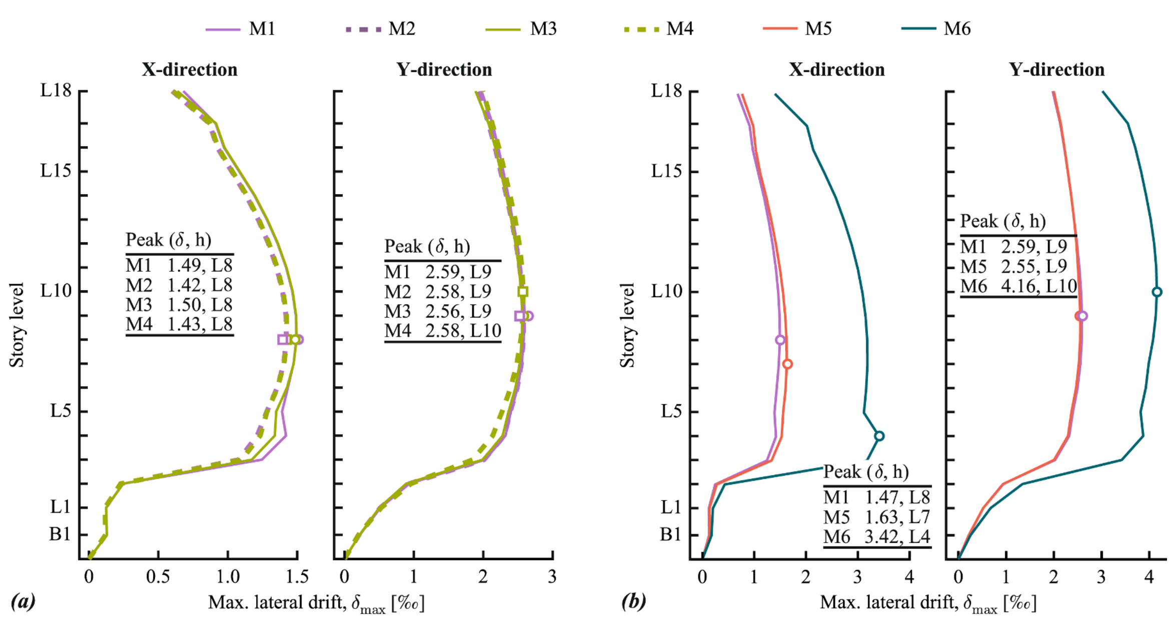

Fig. 20. Comparison of maximum lateral story drift $\delta_{\max}$ for the CM building model due to different model assumptions: (a) Rayleigh damping model effect; and (b) effective stiffness effect.

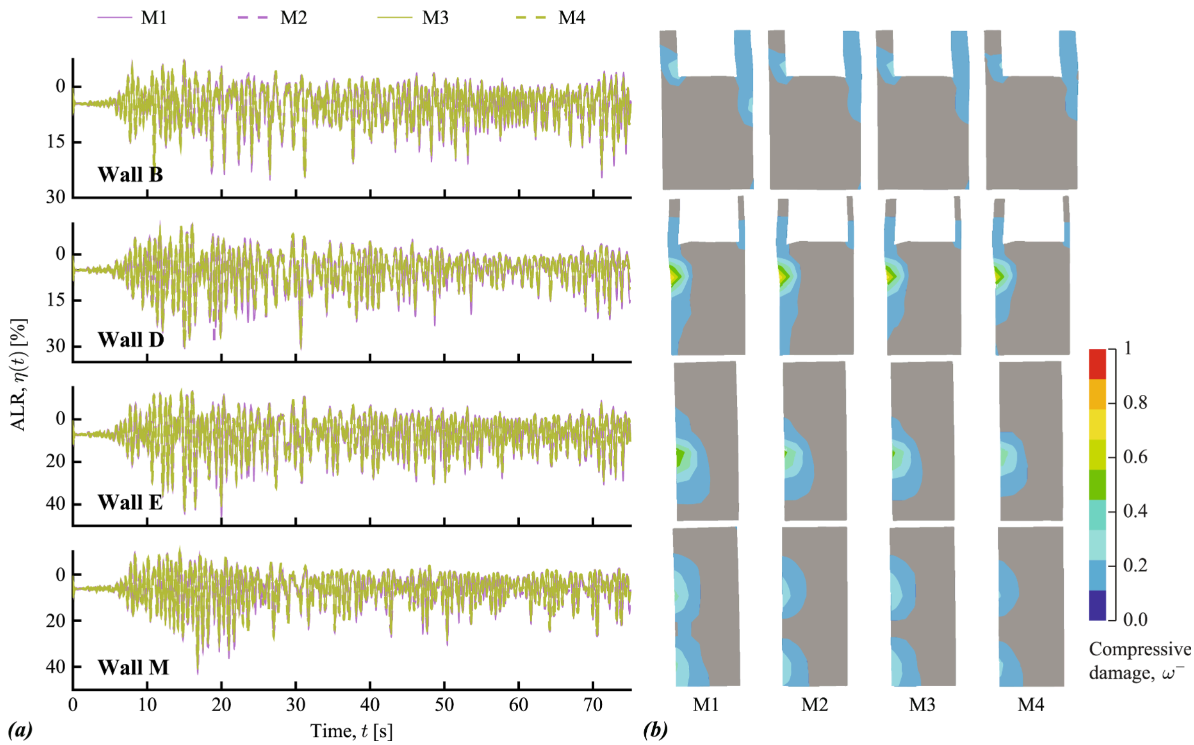

Fig. 21. Comparison of ALR history $\eta(t)$ and compressive damage field ω^- in critical walls of the building due to parameter variation in the Rayleigh's damping model.

Table 11
Peak values of ALR η_{max} and associated times $t_{\eta_{max}}$ of peak in critical walls of the CM model due to parameter variation in the Rayleigh's damping model.

	Peak ALR, η_{max} [%]				Peak time, $t_{\eta_{max}}$ [s]			
Model	B	D	E	M	B	D	E	M
M1	25.2	30.6	45.6	42.8	26.5	15.1	20.0	16.8
M2	24.1	30.5	42.5	38.9	31.2	15.0	15.1	16.8
M3	24.2	30.0	43.1	40.9	31.2	15.1	15.1	16.8
M4	23.5	29.4	40.4	36.4	10.9	15.0	15.1	16.8

while ALR of wall D presents a decrease. Conversely, for model M6, the ALR increases considerably relative to the M1 model, reaching a peak value of 67.9% in wall E, i.e., an increment of 20.9%. For the compressive damage field ω^- in the critical walls (Fig. 22), it is observed that damage does not change significantly between the M5 and M1 model, whereas it increases considerably for the M6 model in magnitude as well as in the extension of the damaged area, which confirms the importance of the slab stiffness.

6.3. Effect of the vertical ground motion component

To analyze the influence of the vertical acceleration ground motion component in the building response, the M1 model (see Table 10) is used with the three ground motion components (XYZ-input), or with just the two horizontal components (XY-input). Results show that differences in this case, in terms of the maximum interstory drift for both cases are negligible; the same observation applies to the compressive damage state ω^-.

Finally, Fig. 23 shows the history of ALR ($\eta(t)$) of walls B and O (located at opposite corners of the building). Results show that for wall B (located at the north end of the building) the ALR decreases its peak by 0.4% if the vertical component is ignored, while for wall O (located at the south end of the building), the ALR increases by 0.4%. The peak occurs at different times in both cases, which means that although the vertical ground motion component does not influence much the magnitude of peak ALR, it does influence the sequence in which each wall reaches its peak ALR value, and hence, the damage observed.

7. Summary and conclusions

This article presents and validates a NRCW model to study the seismic behavior of RC wall buildings. The wall model reproduces well the quasi-static cyclic response of four benchmark RC wall tests, after calibration of the material parameters by a sensitivity analysis. The model was applied to study the inelastic response of a real RC building that underwent severe structural damage during the 2010 Chile earthquake, and the effect of different modeling assumptions was also considered. Results of the model were only compared with experimental tests of walls, which failure mechanism is dominated by bending and compression, and should be extended in the future to include shear failure.

From the analysis performed, it is concluded that modeling of RC wall buildings do not require full inelastic modeling; it only requires to account for the non-linear behavior of the elements in the regions where damage is expected. This reduces the time of analysis considerably. For the elements assumed with elastic behavior, the concrete Young's modulus is calculated using the ACI's equation [48] ($E_c = 4700\sqrt{f_c'}$ in MPa), and the reduction factors of the gross stiffness EI_g using values of 0.70 and 0.25 for walls and slabs, respectively. For the elements with inelastic behavior, the material properties used for the proposed concrete model are: the expected value of f_c'; E_c as for the previous ACI's equation [48]; a value of $2.0f_c'$ for G_c; an f_t value of $0.10f_c'$; 2.0 MPa-mm for G_t; and values of 0 and 0.20 for the plasticity factors in tension and compression ($B^{\pm}$), respectively. For the steel reinforcement bars the used properties are: the expected value for $f_y^{\pm}$; 200 GPa for E_s as suggested by ACI [48]; and 0.03 for $b^{\pm}$. A Rayleigh damping model with a target critical damping ratio of 3% at 0.2 and 1.5 times the fundamental period of the first mode of vibration ($0.2T_1$ and $1.5T_1$) seems to be a

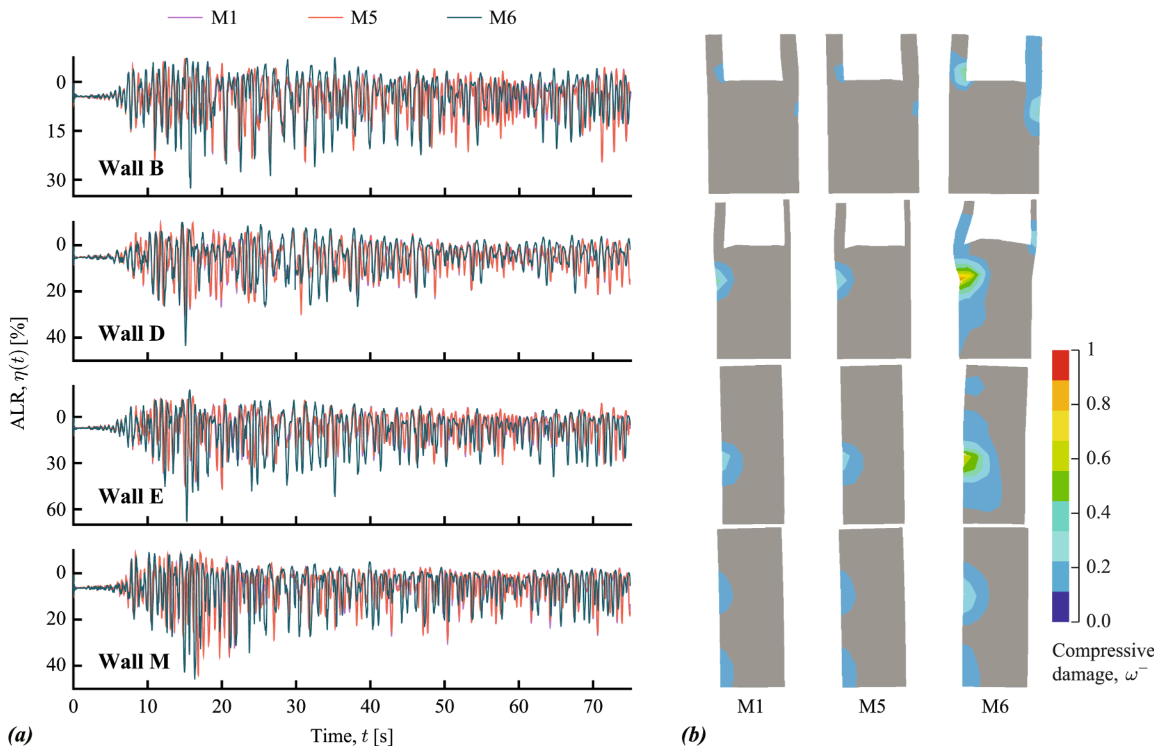

Fig. 22. Comparison of ALR history $\eta(t)$ and compressive damage field ω^- in critical walls of the building due to a variation in the effective bending stiffness of linear elements (walls and slabs).

Table 12
Peak values of ALR η_{max} and associated times $t_{\eta_{max}}$ in critical walls of the building due to variation in the effective bending stiffness of linear elements.

	Peak ALR, η_{max} [%]				Peak time, $t_{\eta_{max}}$ [s]			
Model	B	D	E	M	B	D	E	M
M1	25.2	30.6	45.6	42.4	26.5	15.1	20.1	16.8
M5	25.2	29.9	47.0	44.0	26.5	15.1	20.0	16.8
M6	32.5	43.7	67.9	45.8	15.8	15.1	15.3	16.4

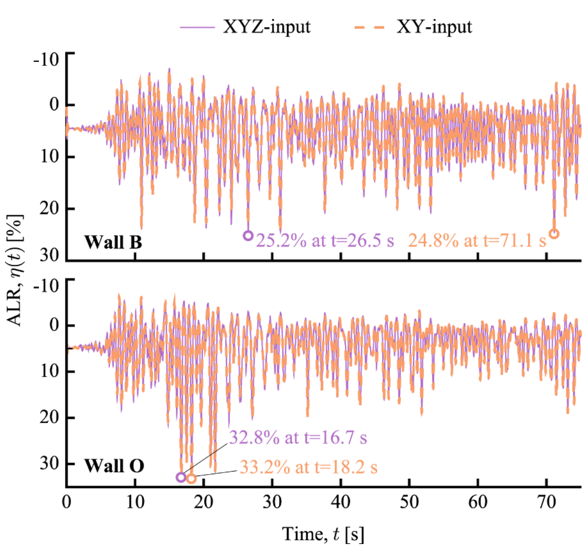

Fig. 23. Comparison of ALR history $\eta(t)$ due to the ground motion vertical component.

reasonable assumption. Additionally, the ground motion vertical component does not significantly affect, in this case, the response of this RC wall building. Some additional specific conclusions are:

- The NRCW model was validated using a database of experimental responses of four slender planar walls tested by four different research groups; two walls with unconfined concrete, and two with confined concrete at the boundary elements. The numerical simulation responses of this study show good agreement with the test results and global response parameters considered, namely, the initial stiffness, peak base shear, peak roof displacement, ultimate base-shear, and dissipated energy. Moreover, good accuracy occurs with local response parameters, such as the compressive damage level, concentration of strains, and damage location.
- A sensitivity analysis performed with the material parameters of the four RC walls shows that the initial stiffness is mainly controlled by the parameters of concrete in tension; the maximum roof displacement (and the ductility of the wall element) depends strongly on the parameters of concrete in compression; and the base-shear forces and the dissipated energy are significantly affected by the post-yield stiffness of the steel reinforcement $b^{\pm}$.
- The building's dynamic behavior and its observed damage pattern are correctly reproduced by the non-linear finite element model. This is important since a similar model could be used to anticipate an undesirable seismic performance in similar RC buildings. As expected, greater displacements occur in the weaker direction of the building. As a result of the building dynamics, the ALR increases significantly in all walls, reaching a peak value of 70%, which highly reduces their ductility.
- The small drift (less than 2‰) values obtained by the structure before it exhibits damage is a symptom of the non-ductile structural behavior, which somewhat contradicts the R factor values used in design.
- Parametric results also indicate that for this structure with limited ductility, the target critical damping ratio ζ_o selected for inelastic

dynamic analysis can slightly modify the seismic response if damage is not significant; however, as damage increases, its value becomes more important in the prediction of the collapse mechanism. A wrong value of ξ can result in overestimating or underestimating floor displacements, and more important, can alter the order in which structural walls get damaged and fail. The authors would like to stress the importance of further research on the effect of damping ratio for structures with limited ductility.

- A reduction in the values of the effective stiffness of elastic walls, leads in this case to a negligible change in the seismic building response. However, changes in the slab bending stiffness are relevant, and lead to double the peak value of story drifts, increase damage in wall damage, and increase the value of ALR up to 50%.
- For this structure, neglecting the vertical component of ground motion may slightly increase (or decrease) the ALR in walls, depending on their physical location within the structure. Peak ALR changes only by $\pm 0.4\%$ between the bidirectional ground motion and the case with three ground motion components. However, these changes do not occur at the same instant. Indeed, the difference between both cases at the instant by peak building response is 3.5%. However, in some of the walls, the effective section is additionally reduced by window or door openings, leading to a increase in the differences. A more comprehensive analysis including other buildings and different earthquake records is recommended to validate these results.

CRediT authorship contribution statement

José A. Gallardo: Conceptualization, Methodology, Investigation, Software, Validation. **Juan C. de la Llera:** Conceptualization, Writing - review & editing, Supervision, Funding acquisition. **Hernán Santa María:** Validation, Supervision. **Matías F. Chacón:** Resources, Methodology, Software, Visualization.

Declaration of Competing Interest

The authors declare that they have no known competing financial interests or personal relationships that could have appeared to influence the work reported in this paper.

Acknowledgments

This research has been sponsored by Ministry of Higher Education, Science, Technology, and Innovation of Ecuador (SENESCYT); FONDECYT project, SImulation Based Earthquake Risk and Resilience of Interdependent Systems and networKs (SIBER-RISK), ANID/ FONDECYT/ 1170836; the Chilean Research Center for Integrated Disaster Risk Management (CIGIDEN), ANID/ FONDAP/ 15110017; and FONDECYT project ANID/ FONDECYT/ 3190680.

Appendix A. Supplementary material

Supplementary data associated with this article can be found, in the online version, at https://doi.org/10.1016/j.engstruct.2021.112093.

References

[1] Wood SL. Performance of reinforced concrete buildings during the 1985 Chile earthquake: implications for the design of structural walls. Earthq Spectra 1991;7 (4):607–38.

[2] Wallace JW, Massone LM, Bonelli P, Dragovich J, Lagos R, Lüders C, Moehle J. Damage and implications for seismic design of RC structural wall buildings. Earthq Spectra 2012;28(S1):S281–99.

[3] Kam WY, Pampanin S, Dhakal R, Gavin H, Roeder C. Seismic performance of reinforced concrete buildings in the September 2010 Darfield (Canterbury) earthquakes. Bull New Zealand Soc Earthq Eng 2010;43(4):340–50.

[4] Kam WY, Pampanin S, Elwood K. Seismic performance of reinforced concrete buildings in the 22 February Christchurch (Lyttleton) earthquake; 2011.

[5] Westenenk B, de la Llera JC, Jünemann R, Hube MA, Besa JJ, Lüders C, Inaudi JA, Riddell R, Jordán R. Analysis and interpretation of the seismic response of RC buildings in Concepción during the February 27, 2010, Chile earthquake. Bull Earthq Eng 2013;11(1):69–91.

[6] Jünemann R, de La Llera J, Hube M, Cifuentes L, Kausel E. A statistical analysis of reinforced concrete wall buildings damaged during the 2010, Chile earthquake. Eng Struct 2015; 82:168–85.

[7] Elwood KJ. Performance of concrete buildings in the 22 February 2011 Christchurch earthquake and implications for Canadian codes. Can J Civ Eng 2013; 40(3):759–76.

[8] Song C, Pujol S, Lepage A. The collapse of the Alto Río building during the 27 February 2010 Maule, Chile, earthquake. Earthq Spectra 2012;28(1_suppl1): 301–34. https://doi.org/10.1193/1.4000036.

[9] Maffei J, Bonelli P, Kelly D, Lehman DE, Lowes L, Moehle J, Telleen K, Wallace J, Willford M. Recommendations for seismic design of reinforced concrete wall buildings based on studies of the 2010 Maule, Chile earthquake, Tech. rep.; 2014.

[10] Deger ZT, Wallace JW. Collapse assessment of the Alto Rio building in the 2010 Chile earthquake. Earthq Spectra 2015;31(3):1397–425. https://doi.org/10.1193/060812EQS209M.

[11] Restrepo J, Conte J, Dunham R, Parker D, Wiesner J, Dechent P. Detailed nonlinear FE pushover analysis of Alto Rio building. In: 16th world conference on earthquake engineering. Santiago, Chile; 2017.

[12] Zhang P, Restrepo JI, Conte JP, Ou J. Nonlinear finite element modeling and response analysis of the collapsed Alto Rio building in the 2010 Chile Maule earthquake. Struct Des Tall Special Build 2017;26(16):e1364.

[13] Westenenk B, de la Llera JC, Besa JJ, Jünemann R, Moehle J, Lüders C, Inaudi JA, Elwood KJ, Hwang S-J. Response of reinforced concrete buildings in Concepción during the Maule earthquake. Earthq Spectra 2012;28(S1):S257–80.

[14] Ugalde D, Lopez-Garcia D. Behavior of reinforced concrete shear wall buildings subjected to large earthquakes. Procedia Eng 2017;199:3582–7.

[15] Lemnitzer A, Massone LM, Skolnik DA, Juan C, Wallace JW. Aftershock response of RC buildings in Santiago, Chile, succeeding the Magnitude 8.8 maule earthquake. Eng Struct 2014;76:324–38.

[16] Vidal F, Navarro M, Aranda C, Enomoto T. Changes in dynamic characteristics of Lorca RC buildings from pre-and post-earthquake ambient vibration data. Bull Earthq Eng 2014;12(5):2095–110.

[17] Dazio A, Beyer K, Bachmann H. Quasi-static cyclic tests and plastic hinge analysis of RC structural walls. Eng Struct 2009;31(7):1556–71.

[18] Tran T. Experimental and analytical studies of moderate aspect ratio reinforced concrete structural walls; 2012. http://search.proquest.com/docview/1115290687/.

[19] Hube M, Marihuén A, De la Llera J, Stojadinovic B. Seismic behavior of slender reinforced concrete walls. Eng Struct 2014;80:377–88.

[20] Amón J. Experimental study of seismic behavior and residual capacity in reinforced concrete slender walls, Master of science thesis. Pontificia Universidad Católica de Chile; 2018 [In Spanish].

[21] Yanez F, Park R, Paulay T. Seismic behaviour of walls with irregular openings. In: Earthquake engineering, world conference, Balkerna, Rotterdam; 1992. p. 3303–8.

[22] Marius M. Seismic behaviour of reinforced concrete shear walls with regular and staggered openings after the strong earthquakes between 2009 and 2011. Eng Fail Anal 2013;34:537–65.

[23] Palermo D, Vecchio FJ, Solanki H. Behavior of three-dimensional reinforced concrete shear walls. ACI Struct J 2002;99(1):81–9.

[24] Thomsen IV JH, Wallace JW. Displacement-based design of slender reinforced concrete structural walls-experimental verification. J Struct Eng 2004;130(4): 618–30.

[25] Li B, Qian K, Wu H. Flange effects on seismic performance of reinforced concrete squat walls with irregular or regular openings. Eng Struct 2016;110:127–44.

[26] Vásquez JA, de la Llera JC, Hube MA. A regularized fiber element model for reinforced concrete shear walls. Earthq Eng Struct Dyn 2016;45(13):2063–83.

[27] Jiang H, Kurama YC. Analytical modeling of medium-rise reinforced concrete shear walls. ACI Struct J 2010;107(4).

[28] Dides MA, De la Llera JC. A comparative study of concentrated plasticity models in dynamic analysis of building structures. Earthq Eng Struct Dyn 2005;34(8): 1005–26.

[29] Orakcal K, Wallace JW, Conte JP. Flexural modeling of reinforced concrete walls-model attributes. Struct J 2004;101(5):688–98.

[30] Chen B, Tan J, Oyang Y. An improved simulation model of shear wall structures of tall building. Procedia Eng 2011; 12:127–32, 2011 SREE Conference on Engineering Modelling and Simulation (CEMS 2011). doi: 10.1016/j.proeng.2011.05.021. http://www.sciencedirect.com/science/article/pii/S1877705811009350.

[31] Pugh JS, Lowes LN, Lehman DE. Nonlinear line-element modeling of flexural reinforced concrete walls. Eng Struct 2015;104:174–92.

[32] Li B, Chen Q. Initial stiffness of reinforced concrete structural walls with irregular openings. Earthq Eng Struct Dyn 2010;39(4):397–417.

[33] Lu Y, Panagiotou M. Three-dimensional cyclic beam-truss model for nonplanar reinforced concrete walls. J Struct Eng 2013;140(3):04013071.

[34] Palermo D, Vecchio FJ. Simulation of cyclically loaded concrete structures based on the finite-element method. J Struct Eng 2007;133(5):728–38.

[35] Kaushik S, Dasgupta K. Seismic damage in shear wall-slab junction in RC buildings. Procedia Eng 2016; 144:1332–9, international Conference on Vibration Problems 2015. doi: 10.1016/j.proeng.2016.05.162. http://www.sciencedirect.com/science/article/pii/S1877705816303794.

[36] Belmouden Y, Lestuzzi P. Analytical model for predicting nonlinear reversed cyclic behaviour of reinforced concrete structural walls. Eng Struct 2007;29(7):1263–76.

[37] Hamburger, R., Deierlein, G. G., Lehman, D. E., Lignos, D. G., Lowes, L. N., Pekelnicky, R., ... & Van de Lindt, J. W. (2017). Recommended modeling

parameters and acceptance criteria for nonlinear analysis in support of seismic evaluation, retrofit, and design. Rep. No. NIST GCR, 17-917.
[38] Almeida JP, Tarquini D, Beyer K. Modelling approaches for inelastic behaviour of RC walls: multi-level assessment and dependability of results. Arch Comput Meth Eng 2016;23(1):69–100.
[39] Chacón MF, Juan C, Hube MA, Marques J, Lemnitzer A. Epistemic uncertainty in the seismic response of RC free-plan buildings. Eng Struct 2017;141:687–702.
[40] Lu X, Lu X, Guan H, Ye L. Collapse simulation of reinforced concrete high-rise building induced by extreme earthquakes. Earthq Eng Struct Dyn 2013;42(5): 705–23.
[41] Lu X, Xie L, Guan H, Huang Y, Lu X. A shear wall element for nonlinear seismic analysis of super-tall buildings using Opensees. Finite Elem Anal Des 2015;98:14–25.
[42] Jünemann R, de la Llera JC, Hube MA, Vásquez JA, Chacón MF. Study of the damage of reinforced concrete shear walls during the 2010 Chile earthquake. Earthq Eng Struct Dyn 2016;45(10):1621–41.
[43] Lu Y, Panagiotou M. Three-dimensional beam–truss model for reinforced concrete walls and slabs–part 2: modeling approach and validation for slabs and coupled walls. Earthq Eng Struct Dyn 2016;45(11):1707–24.
[44] Lu Y, Panagiotou M, Koutromanos I. Three-dimensional beam-truss model for reinforced concrete walls and slabs–part 1: modeling approach, validation, and parametric study for individual reinforced concrete walls. Earthq Eng Struct Dyn 2016;45(9):1495–513.
[45] ASCE, American Society of Civil Engineers. Minimum Design Loads and Associated Criteria for Buildings and Other Structures ASCE/SEI 7-16; 2017. doi: 10.1061/9780784414248.
[46] ASCE, American Society of Civil Engineers. Seismic Evaluation and Retrofit of Existing Buildings. ASCE/SEI 41-17; 2017. doi: 10.1061/9780784414859.
[47] FEMA. NEHRP Recommended seismic provisions for new buildings and other structures (FEMA P-1050-1), 2015.
[48] ACI. 318, Building code requirements for structural concrete (ACI 318-19): An ACI standard: Commentary on building code requirements for structural concrete (ACI 318R-19), American Concrete Institute; 2019.
[49] Cruz C, Miranda E. Evaluation of the Rayleigh damping model for buildings. Eng Struct 2017;138:324–36.
[50] Michel C, Guéguen P, Bard P-Y. Dynamic parameters of structures extracted from ambient vibration measurements: An aid for the seismic vulnerability assessment of existing buildings in moderate seismic hazard regions. Soil Dyn Earthq Eng 2008;28(8):593–604.
[51] Smyrou E, Priestley MN, Carr AJ. Modelling of elastic damping in nonlinear time-history analyses of cantilever RC walls. Bull Earthq Eng 2011;9(5):1559–78.
[52] ANSYS, Release 19.2, ANSYS Inc.
[53] Faria R, Oliver J, Cervera M. A strain-based plastic viscous-damage model for massive concrete structures. Int J Solids Struct 1998;35(14):1533–58.
[54] Menegotto M, Pinto P. Method of analysis for cyclically loaded reinforced concrete plane frames including changes in geometryand non-elastic behavior of elements under combined normal force and bending. In: Proceedings. IABSE sympoium on resistance and ultimate deformability of structures acted on by well-defined repeated loads.
[55] Bathe K-J, Dvorkin EN. A formulation of general shell elements–the use of mixed interpolation of tensorial components. Int J Numer Meth Eng 1986;22(3):697–722.
[56] Gallardo Briones JA. Finite element collapse analysis of a residential reinforced concrete wall building during the 2010, Maule earthquake, Master of Science thesis. Pontificia Universidad Católica de Chile; 2019.
[57] Ortiz M. A constitutive theory for the inelastic behavior of concrete. Mech Mater 1985;4(1):67–93.
[58] Chacón MF. Epistemic uncertainty of linear building models and inelastic continuum concrete models. Ph.D. thesis. Santiago, Chile: Pontifical University Catholic of Chile; 2018.
[59] Simo JC, Ju J. Strain-and stress-based continuum damage models–i. Formulation. Int J Solids Struct 1987;23(7):821–40.
[60] Faria R, Oliver J, Ruiz MC. On isotropic scalar damage models for the numerical analysis of concrete structures. Spain: Centro Internacional de Métodos Numéricos en Ingeniería Barcelona; 2000.
[61] Duvaut G, Lions JL. Les inéquations en mécanique et en physique; 1972.
[62] Razvi S, Saatcioglu M. Confinement model for high-strength concrete. J Struct Eng 1999;125(3):281–9.
[63] Oliver J, Cervera M, Oller S, Lubliner J. Isotropic damage models and smeared crack analysis of concrete. In: Proc. SCI-C computer aided analysis and design of concrete structures, vol. 945958; 1990.
[64] Filippou FC, Bertero VV, Popov EP. Effects of bond deterioration on hysteretic behavior of reinforced concrete joints; 1983.
[65] Elmorsi M, Kianoush MR, Tso W. Nonlinear analysis of cyclically loaded reinforced concrete structures. Struct J 1998;95(6):725–39.
[66] Orakcal K, Sanchez LMM, Wallace JW. Analytical modeling of reinforced concrete walls for predicting flexural and coupled-shear-flexural responses, Pacific Earthquake Engineering Research Center, College of Engineering; 2006.
[67] Wu JY, Li J, Faria R. An energy release rate-based plastic-damage model for concrete. Int J Solids Struct 2006;43(3–4):583–612.
[68] Nakamura H, Higai T. Compressive fracture energy and fracture zone length of concrete, Modeling of inelastic behavior of RC structures under seismic loads; 2001:471–87.
[69] Instituto Nacional de Normalización (INN), 1996. Diseño Sísmico de Edificios, NCh433Of.96, Santiago, Chile (in Spanish).
[70] DICTUC. Estudios de evaluación y diagnóstico estructural de edificios siniestrados por el terremoto del 27 de Febrero de 2010, Santiago, Chile (in spanish), Tech. rep.; 2010.
[71] Computers and Structures, Etabs, v9.7.4, Computers and Structures Inc.
[72] Chopra AK. Dynamics of structures 4th ed; 2012.